

Neuron

Closed-Loop Real-Time Imaging Enables Fully Automated Cell-Targeted Patch-Clamp Neural Recording *In Vivo*

Highlights

- Imagepatching enables fully automated cell-targeted patch-clamp recording *in vivo*
- Closed-loop real-time imaging accounts for target cell movements during patching
- Successful whole-cell recordings are obtained from targeted neurons *in vivo*

Authors

Ho-Jun Suk, Ingrid van Welie, Suhasa B. Kodandaramaiah, Brian Allen, Craig R. Forest, Edward S. Boyden

Correspondence

esb@media.mit.edu

In Brief

The imagepatcher developed by Suk et al. fully automates cell-targeted patch-clamp recordings *in vivo*. The system can obtain successful whole-cell recordings from targeted neurons in the intact brain without human intervention, with yield comparable to skilled human experimenters.



Closed-Loop Real-Time Imaging Enables Fully Automated Cell-Targeted Patch-Clamp Neural Recording *In Vivo*

Ho-Jun Suk,^{1,2,3} Ingrid van Welie,^{2,3} Suhasa B. Kodandaramaiah,^{2,3} Brian Allen,^{2,3} Craig R. Forest,⁴ and Edward S. Boyden^{2,3,5,6,7,*}

¹Health Sciences and Technology

²Media Lab

³McGovern Institute

Massachusetts Institute of Technology, Cambridge, MA 02139, USA

⁴G.W. Woodruff School of Mechanical Engineering, Georgia Institute of Technology, Atlanta, GA 30332, USA

⁵Department of Brain and Cognitive Sciences

⁶Department of Biological Engineering

Massachusetts Institute of Technology, Cambridge, MA 02139, USA

⁷Lead Contact

*Correspondence: esb@media.mit.edu

<http://dx.doi.org/10.1016/j.neuron.2017.08.011>

SUMMARY

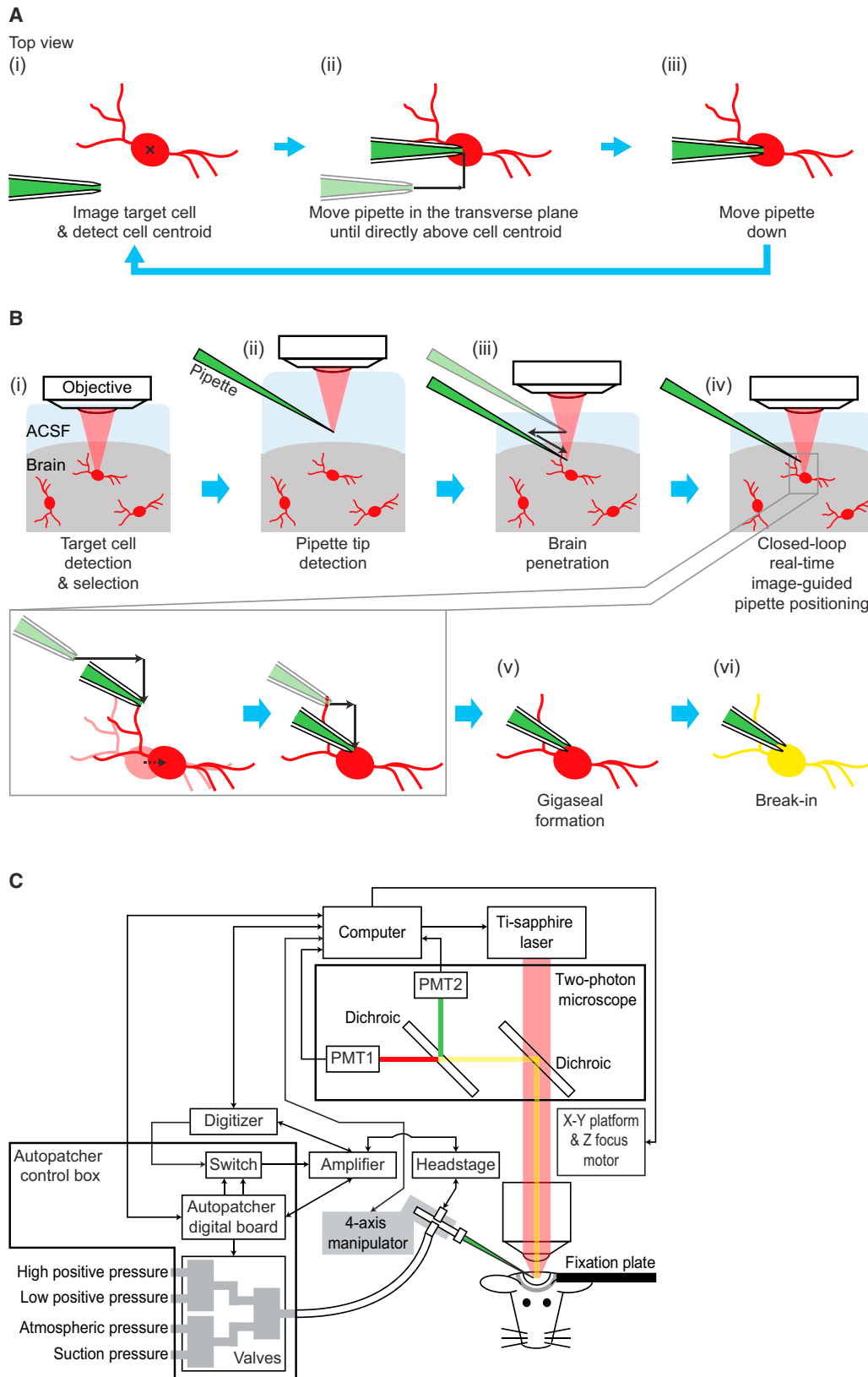
Targeted patch-clamp recording is a powerful method for characterizing visually identified cells in intact neural circuits, but it requires skill to perform. We previously developed an algorithm that automates “blind” patching *in vivo*, but full automation of visually guided, targeted *in vivo* patching has not been demonstrated, with currently available approaches requiring human intervention to compensate for cell movement as a patch pipette approaches a targeted neuron. Here we present a closed-loop real-time imaging strategy that automatically compensates for cell movement by tracking cell position and adjusting pipette motion while approaching a target. We demonstrate our system’s ability to adaptively patch, under continuous two-photon imaging and real-time analysis, fluorophore-expressing neurons of multiple types in the living mouse cortex, without human intervention, with yields comparable to skilled human experimenters. Our “imagepatching” robot is easy to implement and will help enable scalable characterization of identified cell types in intact neural circuits.

INTRODUCTION

Targeted patch-clamp recording of visually identified neurons (Dittgen et al., 2004; Kitamura et al., 2008; Margrie et al., 2003) is a powerful technique for electrophysiological characterization of cells of a given class in the living mammalian brain and is in increasing demand for its ability to link a cell’s molecular and anatomical identity with its electrophysiological characteristics

in the context of specific behaviors, states, and diseases (Chen et al., 2015; Li et al., 2015; Pala and Petersen, 2015; Runyan et al., 2010; van Welie et al., 2016). However, the manual labor and skill required to perform visually guided patching *in vivo* have limited widespread adoption of the technique. Previously, we discovered that non-image guided (i.e., “blind”) patching *in vivo* could be reduced to an algorithm, and we accordingly built a robot, which we called the “autopatcher,” that automatically performs blind patch-clamp recordings of single neurons in the intact brain by detecting cells based on changes in pipette tip impedance (Kodandaramaiah et al., 2012, 2016). Since then, several attempts have been made to automate visually guided patch-clamp recordings of targeted neurons. Although these attempts have enabled automatic positioning of a patch pipette near a visually identified neuron, all currently available systems either need a human to perform the final patching process itself (Long et al., 2015) or require human adjustment of the patching process for about half of the trials (Wu et al., 2016). We realized that a system that can achieve the whole-cell patch-clamp configuration from a targeted cell without human intervention needs to address a key technical challenge: as a patch pipette moves toward a target cell for patch clamping, the cell moves as well, causing the pipette to miss its mark without manual adjustments of pipette motion that compensate for cell movement.

We therefore designed a new kind of algorithm, which we call “imagepatching,” in which real-time imaging in a closed-loop fashion allows for continuous adaptation of the pipette trajectory in response to changes in cell position throughout the patching process. We constructed a simple robotic system and software suite implementing imagepatching that can operate on a conventional two-photon microscope with commercially available manipulators and amplifiers, and show that we can obtain *in vivo* patch-clamp recordings from fluorescently labeled neurons, of multiple cell types, in the living mouse cortex without any human intervention, and with a quality and yield similar to or even



(legend on next page)

exceeding that obtained by skilled human experimenters. Our imagepatching robot is easy to implement and will help enable scalable electrophysiological characterization of identified cell types in intact neural circuits.

RESULTS

Closed-Loop Real-Time Imaging Algorithm for Compensation of Target Cell Movement during Image-Guided Patch Clamping

In the anesthetized mouse cortex, we found that moving a patch pipette by 300–400 μm from above the brain surface into layer 2/3 along the axial direction (i.e., parallel to the pipette axis, 30° below the horizontal) resulted in a target cell displacement of $6.8 \pm 5.1 \mu\text{m}$ (mean \pm SD used throughout; $n = 25$ cells in 6 mice; Figure S1A) in the transverse plane. In addition, we observed that pipette navigations in the vicinity of a targeted cell (i.e., pipettes moving by ~ 5 – $10 \mu\text{m}$ when starting ~ 20 – $30 \mu\text{m}$ away from the cell) caused the targeted cell to move by $2.2 \pm 1.4 \mu\text{m}$ ($n = 27$ cells in 17 mice; Figure S1B) in the transverse plane. These findings suggested that to correctly place the pipette tip on a targeted cell and patch it in a fully automated fashion, the displacement of the target cell resulting from pipette movement needs to be compensated for as the pipette is advanced toward the cell. Accordingly, we developed a closed-loop real-time image-guided algorithm that involves repeated target cell imaging followed by centroid detection (Figure 1Ai) and pipette movement (Figures 1Aii and 1Aiii) stages, to continuously compensate for cell movement as the pipette approaches the target. We found that with the closed-loop algorithm supporting pipette navigation to a targeted cell, the entire image-guided patching process could be reduced to a six-stage “imagepatching” algorithm (Figure 1B; full flowchart in Figure S2). Imagepatching fuses closed-loop real-time image-guided pipette positioning with our earlier impedance-based cell detection strategy (Kodandaramaiah et al., 2012, 2016) to enable automated cell-attached or whole-cell patch-clamp recording of visually identified cells in the intact mammalian brain.

To implement imagepatching, we built a robotic system (“imagepatcher”) on a commercial two-photon microscope, which we controlled using ScanImage software (Pologruto et al., 2003) integrated with our MATLAB code that performs the real-time closed-loop image analysis. We chose ScanImage as the core software for the imagepatcher, since it works with two-photon systems from multiple vendors and because its open code allowed us to incorporate real-time analysis of ScanImage-acquired images. The imagepatcher hardware

shown in Figure 1C was assembled by augmenting a conventional two-photon image-guided patch-clamp rig with an autopatcher control box (Kodandaramaiah et al., 2012, 2016) that was modified to provide a wide range of pressure values (see STAR Methods for details of this, as well as other technical implementation points summarized in the following section). We validated the imagepatcher by using it to obtain targeted *in vivo* recordings from tdTomato-expressing cells in somatosensory and motor cortices of anesthetized Cre-dependent reporter mice, namely parvalbumin (PV)-positive interneurons in PV-Cre x Ai14 mice and calcium/calmodulin-dependent protein kinase II isoform alpha (CaMKII α)-positive pyramidal neurons in CaMKII α -Cre x Ai14 mice (Clarke, 1993; Hippenmeyer et al., 2005; Tsien et al., 1996). PV-positive and CaMKII α -positive cells had different cortical densities (9.6 ± 6.3 tdTomato-expressing cells per volume of $200 \times 200 \times 100 \mu\text{m}^3$ in 9 PV-Cre x Ai14 mice versus 47.0 ± 31.8 tdTomato-expressing cells in this volume in 7 CaMKII α -Cre x Ai14 mice) and morphologies (example two-photon images of tdTomato-expressing cells in layer 2/3 somatosensory cortex of each mouse line are shown in Figures 4A and 4B) and thus allowed us to explore the degree of generality that the imagepatcher offers to an end user.

Imagepatcher Operation

The imagepatcher starts by executing a target cell detection and selection stage (Figure 1Bi), in which two-photon images of the mouse brain are acquired and then analyzed to identify fluorescent cells. From these candidate cells, the end user can select a neuron of interest using the imagepatcher’s graphical user interface (see Methods S1, related to STAR Methods, in the Supplemental Information for details). The imagepatcher then moves on to the pipette tip detection stage (Figure 1Bii), where a dye (e.g., Alexa 488)-filled patch pipette is brought into the field of view above the brain, and the tip of the patch pipette is automatically located. The pipette tip is identified using a pipette tip detection algorithm (Figure 2A) derived from our finding that the cluster of bright pixels in the pipette image (Figure 2Aii, area bounded by yellow outline), which represents the fluorescence from the dye inside the pipette, robustly changes its position as the focal plane of the microscope objective is moved downward from above the pipette tip. Accordingly, we developed a pipette tip detection algorithm to acquire a z stack around the pipette tip (Figure 2Ai) and to identify the image in the stack capturing the cluster of bright pixels that is furthest away from the far end of the pipette (represented by the centroid of the cluster in the topmost image in the stack; Figure 2Aii.i, black x), assigning the z coordinate of this farthest-cluster image as the z coordinate of the pipette tip (Figure 2Aii, z_{pipette}). The portion of the pipette

Figure 1. Imagepatching: Closed-Loop Real-Time Image-Guided Patch Clamping *In Vivo*

(A) The closed-loop algorithm for continuous cell centroid localization and pipette position adjustment while approaching the targeted cell (for step-by-step flowchart, see Figure S2). Green, patch pipette filled with fluorescent dye; red, fluorescent cell targeted for patching; black x, target cell centroid; black arrows, pipette movement.

(B) The six stages of the image-guided automated patching algorithm (for step-by-step flowchart, see Figure S2). ACSF, artificial cerebrospinal fluid; red, fluorescent cells; green, patch pipette filled with fluorescent dye; light red, laser for two-photon imaging; black solid arrows, pipette movements; black dotted arrow, cell movement; yellow, target cell filled with the fluorescent dye from the pipette.

(C) Schematic of the imagepatcher hardware, composed of a conventional two-photon image-guided patch-clamp rig and our previously developed autopatcher control box (Kodandaramaiah et al., 2012, 2016). Arrows indicate the direction of information flow. PMT, photomultiplier tube.

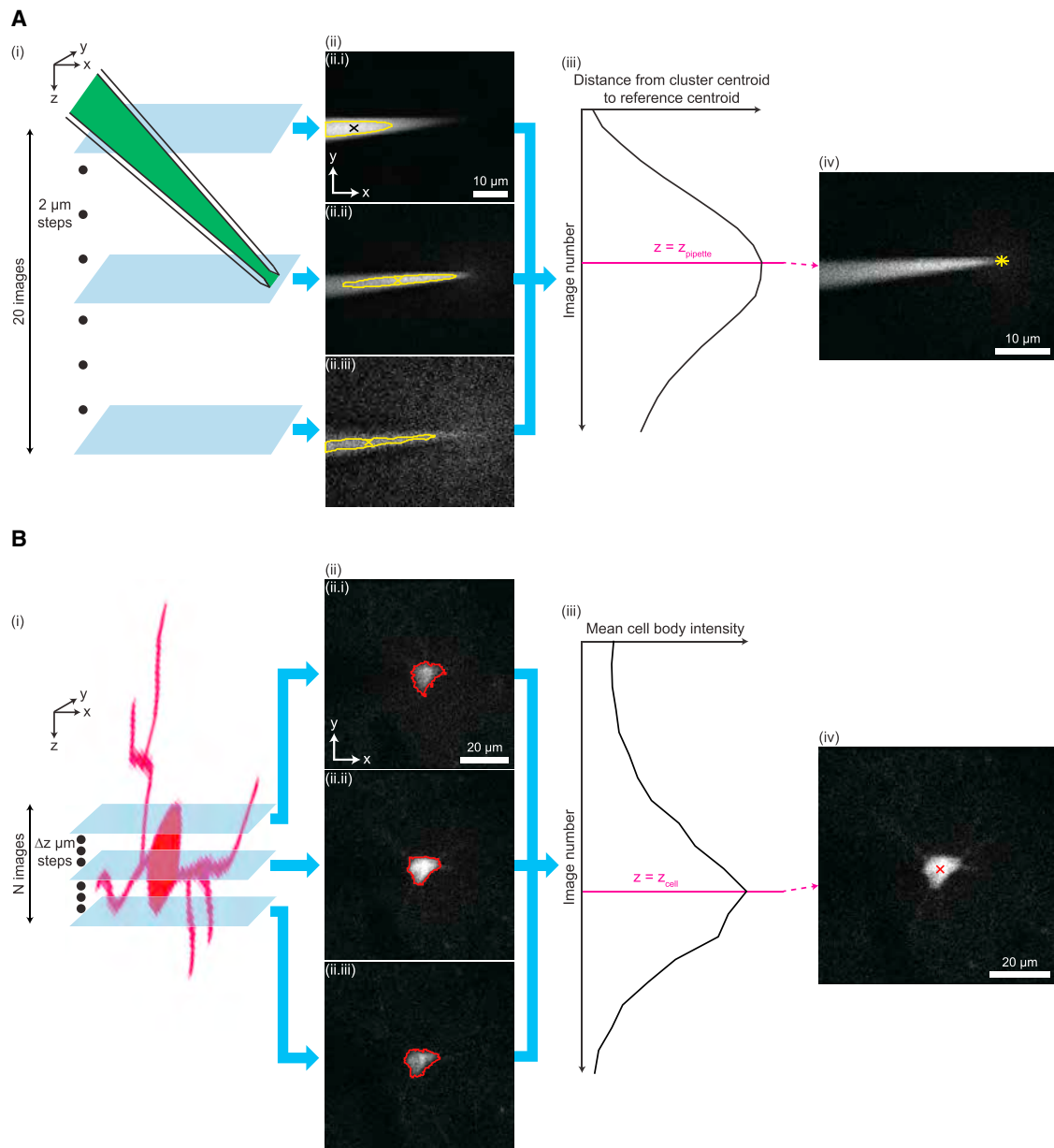


Figure 2. Key Algorithms for Closed-Loop Real-Time Image Analysis

(A) Steps of the pipette tip detection algorithm. (Ai) A z stack with 20 images and $2\ \mu\text{m}$ step between consecutive images is acquired around a pipette filled with a dye (e.g., Alexa 488, green). (Aii) Each image in the z stack is analyzed to identify the cluster of bright pixels (area bounded by yellow outline, corresponding to the fluorescence from Alexa 488 inside the pipette) and the centroid of the cluster (x). The centroid in the topmost image of the z stack (Aii.i, black x) is used as a reference location corresponding to the far end (i.e., end opposite to the pipette tip) of the pipette. Images 1 (Aii.i), 10 (Aii.ii), and 20 (Aii.iii) of the z stack, numbered from top to bottom, are shown as examples. (Aiii) The distance between the cluster centroid (x in Aii) and the reference centroid (black x in Aii.i) is calculated for each image in the z stack. The image at which this distance is the largest is identified as the image focused on the pipette tip (magenta line). The z-coordinate of the focused image corresponds to that of the pipette tip (z_{pipette}). (Aiv) The image focused on the pipette tip is analyzed to yield the location of the pipette tip in the transverse plane (yellow star). For image analysis steps used to locate the pipette tip in the transverse plane, see Figure S3A.

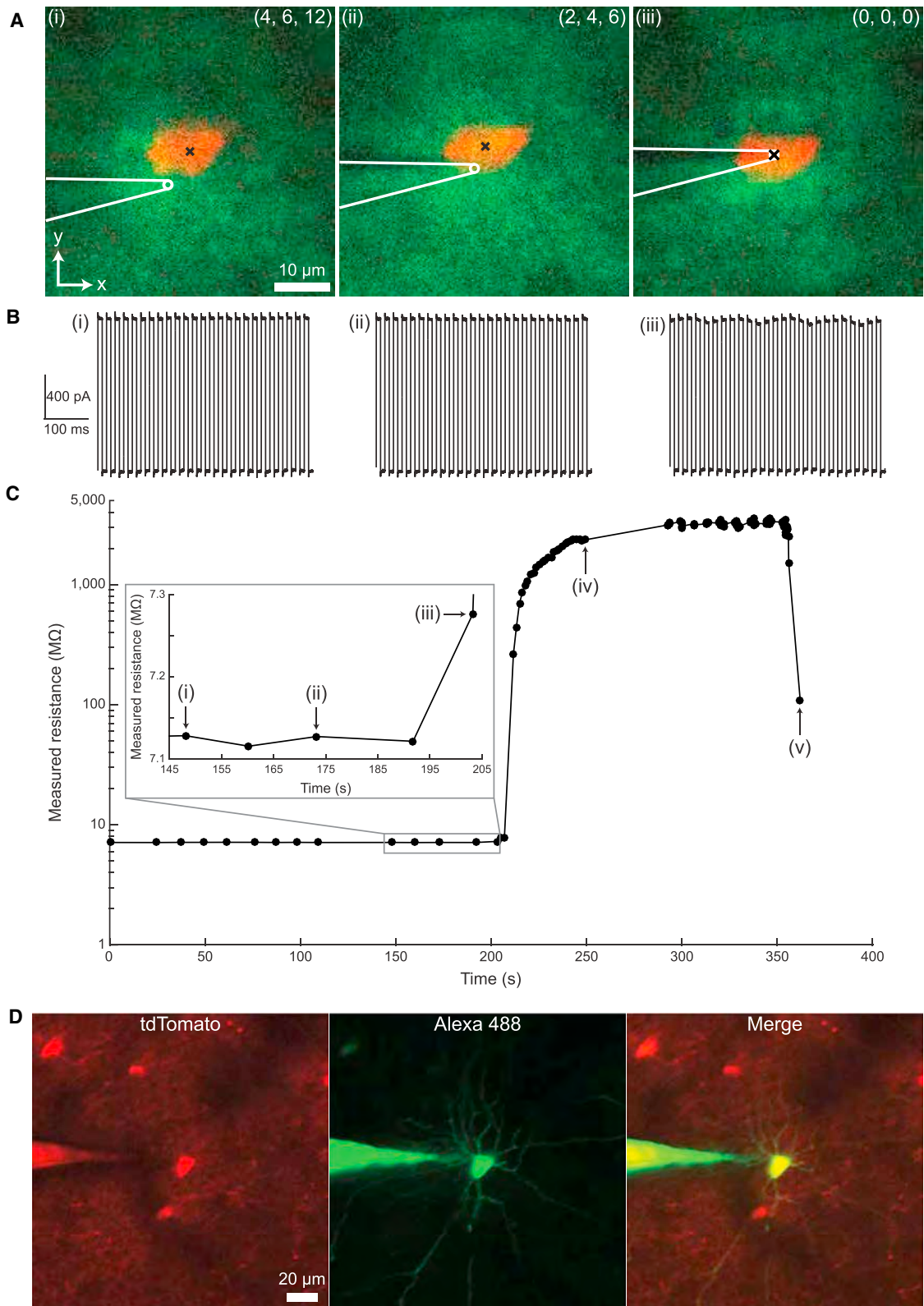
(B) Steps of the cell position detection algorithm. (Bi) A z stack is acquired around a tdTomato-expressing cell (red), with N images and Δz step between consecutive images ($N = 25$, $\Delta z = 3\ \mu\text{m}$ for cell position detection in the brain penetration stage; $N = 15$ or 25 , $\Delta z = 2\ \mu\text{m}$ for cell position detection in the closed-loop real-time image-guided pipette positioning stage). (Bii) Each image in the z stack is analyzed to detect the boundary of the cell body (red outline). Images 8 (Bii.i), 12 (Bii.ii), and 16 (Bii.iii) of the z stack, numbered from top to bottom, are shown as examples. (Biii) The mean intensity of pixels representing the cell body (i.e., pixels surrounded by the detected boundary in Bii) is calculated for each image in the z stack. The image at which this mean intensity is the highest is identified as the image focused on the centroid of the cell body (magenta line). The z-coordinate of the focused image corresponds to that of the cell centroid (z_{cell}). (Biv) The image corresponding to the z-coordinate of the cell centroid is analyzed to yield the centroid position in the transverse plane (red x). For image analysis steps used to detect the boundary and the centroid of the cell body, see Figure S3B.

tip detection algorithm responsible for the identification of the pipette tip in the image at z_{pipette} (Figure 2Aiv) was developed based on the fact that an image focused on the pipette tip shows a triangular object corresponding to the pipette shank converging to a point (i.e., the pipette tip). We therefore designed the pipette tip detection algorithm to find the cluster of bright pixels that captures three vertices of the pipette from the image at z_{pipette} (Figure S3Aii.ii), which is then analyzed to identify the pixel corresponding to the pipette tip (Figure S3Aiii). When tested on 16 z stacks (2 μm step size, 20 images, 17 \times zoom), each of which captured the tip of a separate Alexa 488-filled patch pipette (angled at 30° below the horizontal) at a distinct position within the stack, the pipette tip detection algorithm was capable of accurately extracting the pipette tip, with the tip location determined by the algorithm deviating from the visually assessed tip position by $-1.0 \pm 0.8 \mu\text{m}$, $-0.2 \pm 0.4 \mu\text{m}$, and $1.0 \pm 2.4 \mu\text{m}$ in the x, y, and z directions, respectively. The algorithm's performance was similar for patch pipettes at different angles below the horizontal (see STAR Methods, "Performance of the pipette tip detection algorithm at angles other than 30° below the horizontal," for details).

The pipette tip location determined during the pipette tip detection stage is used by the imagepatcher to compute the ideal trajectory to the target cell at the start of the brain penetration stage (Figure 1Biii), and also to calculate the pipette tip position in subsequent stages of imagepatching; we decided not to utilize the pipette tip detection algorithm (Figure 2A) to locate the pipette tip from the brain penetration stage onward, because a pipette that entered the brain without contamination ejected a plume of fluorescent dye that obscured the exact location of the pipette tip, which made it difficult to robustly resolve the pipette tip using an image-based algorithm. To enter the brain, the imagepatcher applies high positive pressure (600 mBar) to the pipette and moves it along the calculated trajectory at about 600 $\mu\text{m}/\text{s}$ (i.e., at the maximum speed that our four-axis micromanipulator can generate under software control; the same speed is used to move the pipette throughout imagepatcher operation) until the pipette tip is within 75 μm from the initial target cell location. At this point, the pipette pressure is quickly reduced to 300 mBar to prevent excessive background fluorescence, but if little or no dye is ejected around the pipette tip, or a drastic resistance increase is observed, the pipette is deemed contaminated and brief pulses of positive pressure (>300 mBar) are applied to clean the pipette tip (as described in Komai et al., 2006). The pressure value of the pulse is increased until the pipette tip is cleared, but no more than 800 mBar is applied, as a pipette ejecting the dye at this high pressure can cause excessive background fluorescence that interferes with cell detection in subsequent steps of imagepatcher operation. If the clogged state persists even after two pulses of high positive pressure, the contaminated pipette is automatically retracted. For an uncontaminated or a cleared pipette, the imagepatcher applies a pipette pressure of 300 mBar while moving the pipette tip to the vicinity of the target, as we found this pressure value to be high enough to keep the pipette tip clean inside the brain, but not so high as to cause a lingering flood of dye that would lead to excessive background fluorescence (see STAR Methods, "Derivation of pipette pressure for brain entry and cell approach," for details).

Once the pipette tip is within 50 μm from the target cell's initial location, the imagepatcher re-images and re-detects the target cell to account for cell movement resulting from pipette entry into the brain, using the cell position detection algorithm described in Figure 2B. The algorithm was derived based on the fact that in fluorescence microscopy, a fluorescent object looks the brightest when it is in focus (i.e., an image of a fluorescently labeled cell captures pixels corresponding to the fluorescence of the cell, and these pixels have higher intensities in an image focused on the cell compared to out-of-focus images). We thus built the cell position detection algorithm to detect the cell body in each image of a z stack of the target cell (Figure 2Bii) and then to identify the image with the highest mean pixel intensity within the cell body (Figure 2Biii, magenta line), which yields the z-coordinate of the target cell (Figure 2Biii, z_{cell}). We also designed the cell position detection algorithm to identify the centroid (i.e., center of mass) of the cell body in the image at z_{cell} (Figure 2Biv, red x), which is then assigned as the cell position in the transverse plane, because the cell body centroid is where investigators manually performing image-guided patching would aim with the tip of a patch pipette (Häusser and Margrie, 2014; Komai et al., 2006). When tested on 21 z stacks (2 or 3 μm step size, 15 or 25 images, 17 \times zoom; from five mice), each capturing a PV-positive neuron at a different position within the cortex, the cell position detection algorithm correctly yielded x, y, and z coordinates of the cell centroid in all 21 stacks (visually assessed). Following cell position detection, the pipette is moved so that its tip is 25 μm above the updated target cell centroid, and the pipette tip is checked again for contamination.

With the clean pipette tip in place, the closed-loop real-time image-guided pipette positioning stage (Figure 1Biv) begins by lowering the pipette pressure (to 100 mBar) to prevent the target cell from being blown out of place and by performing another cell position detection (as in Figure 2B) to update the location of the target cell. The imagepatcher then repeatedly finds the target cell centroid (Figures 1Ai and 2Biv) and repositions the pipette in the transverse plane according to the offset from the pipette tip to the cell centroid (Figure 1Aii) before each downward 3 μm z-step toward the target cell (Figure 1Aiii; example data from multiple steps of this closed-loop operation are in Figures 3A and 3B, with corresponding imagepatching impedance trajectory in Figure 3C). Similar to manual image-guided patching *in vivo* (Häusser and Margrie, 2014; Komai et al., 2006; Margrie et al., 2003), both visual (pipette tip within the boundary of the target cell soma; Figure 3Aiii) and electrical (resistance increase that exceeds a certain threshold; Figure 3Ciii) parameters are repeatedly checked while the pipette advances toward the target cell to determine when the pipette tip touches the target cell membrane. The imagepatcher maintains the pipette pressure at 100 mBar until the pipette tip makes contact with the cell membrane, because we found that this pressure helped prevent pipette tip clogging and allowed a detectable change in pipette resistance to be observed when the pipette tip touched the cell membrane (as in Figure 3Ciii), while not blowing the target cell out of place and not resulting in excessive background fluorescence (see STAR Methods, "Derivation of pipette pressure for brain entry and cell approach" and "Optimization of cell-pipette contact detection, gigaseal formation, and



(legend on next page)

break-in," for details). Once the pipette tip makes contact with the cell membrane, the imagepatcher dynamically changes the pipette pressure from 100 mBar to 30 mBar to prepare for gigaseal formation. We found that this lowering of pressure resulted in reduction of, and fluctuation of, the amplitude of current pulses that were observed in response to the application of voltage steps to the pipette tip, corresponding to the heartbeat modulation that has been reported previously (Häusser and Margrie, 2014; Komai et al., 2006; Margrie et al., 2003). We also found that the amount of amplitude reduction, which we computed by comparing the pipette resistance before and after the pressure change, and the amount of amplitude fluctuation, which we quantified by calculating the SD of the amplitude of current pulses, were useful predictors of gigaseal formation when they each exceeded a certain threshold (see STAR Methods, "Optimization of cell-pipette contact detection, gigaseal formation, and break-in," for details). The imagepatcher therefore checks if resistance change and the SD of the current pulse amplitude following the lowering of pipette pressure to 30 mBar are high enough before advancing to the gigaseal formation stage (Figure 1Bv).

During gigaseal formation, the positive pressure is removed and 20 mBar suction is applied while hyperpolarizing the pipette. When a gigaohm seal is established (Figure 3Civ), the imagepatcher operation may be halted to obtain cell-attached extracellular recordings. For whole-cell mode, the imagepatcher advances to the break-in stage (Figure 1Bvi), in which increasing pulses of suction (starting at 25 mBar and increasing up to 350 mBar) are applied to achieve the whole-cell configuration (Figure 3Cv). As done at the completion of manual image-guided patching *in vivo* (Häusser and Margrie, 2014; Komai et al., 2006; Margrie et al., 2003), the imagepatcher checks if the dye from the pipette is filling the target cell, by first acquiring a z stack around the target cell, then identifying pixels corresponding to the cell body (as in Figure 2Bii), and finally calculating the mean pixel intensity of the cell body in the microscope channel corresponding to the pipette dye, to verify successful break-in (an example of a dye-filled cell at the end of successful imagepatching is shown in Figure 3D).

Imagepatcher Performance

Using the imagepatcher, stable cell-attached extracellular and whole-cell intracellular recordings could be obtained from PV-positive neurons (example recordings in Figures 4C and 4E) and CaMKII α -positive neurons (example recordings in Figures 4D and 4F) in layer 2/3 of somatosensory and motor cortices of anesthetized mice, enabling *in vivo* observations of supra- and

subthreshold activities of these cells. Access resistance, resting potential, and holding current (Figures 4G–4I) of imagepatched cells ($n = 24$ PV-positive neurons from 14 PV-Cre x Ai14 mice and 13 CaMKII α -positive neurons from seven CaMKII α -Cre x Ai14 mice) were comparable to those reported by previous studies involving two-photon image-guided patching of cortical neurons *in vivo* (Atallah et al., 2012; Gentet et al., 2010, 2012; Mateo et al., 2011; Pala and Petersen, 2015) and were not significantly different from the cells that we manually patched ($n = 11$ PV-positive neurons from 8 PV-Cre x Ai14 mice; Figures S4A–S4C; $p = 0.49$ for access resistance, $p = 0.08$ for resting potential, $p = 0.19$ for holding current when comparing imagepatched and manually patched PV-positive cells; two-sided Student's *t* test with 95% confidence level, assuming unknown and unequal variances). Other properties of imagepatched neurons, such as input resistance and spontaneous firing rate (Figures S4D and S4E; $n = 9$ PV-positive neurons from 5 PV-Cre x Ai14 mice and 13 CaMKII α -positive neurons from seven CaMKII α -Cre x Ai14 mice), also showed distributions of values that overlapped with those obtained in previous *in vivo* studies of cortical neurons (Mateo et al., 2011; Pala and Petersen, 2015).

The imagepatcher obtained targeted patch-clamp recordings in 10 ± 3 min from the brain penetration stage onward ($n = 24$ PV-positive neurons from 14 PV-Cre x Ai14 mice and 13 CaMKII α -positive neurons from seven CaMKII α -Cre x Ai14 mice; each of the two preceding stages of the algorithm takes around 1–2 min extra), with the recordings lasting for 7–30 min for PV-positive neurons ($n = 9$ cells, 5 PV-Cre x Ai14 mice; Figure 4J) and 5–41 min for CaMKII α -positive neurons ($n = 13$ cells, seven CaMKII α -Cre x Ai14 mice; Figure 4J). When targeting PV-positive cells, the gigaohm seal was obtained 42 times out of 108 attempts, and 24 of the 42 gigaohm seals successfully led to the whole-cell configuration (from 17 PV-Cre x Ai14 mice, of which 16 yielded one or more gigaohm seals and 14 yielded one or more whole-cell configurations). For CaMKII α -positive cells, from 65 trials, the gigaohm seal was achieved 19 times, out of which the whole-cell configuration was achieved 13 times (from 10 CaMKII α -Cre x Ai14 mice, of which 10 yielded one or more gigaohm seals and seven yielded one or more whole-cell configurations). These success rates (for PV-positive neurons, 38.9% for obtaining gigaohm seals, and 22.2% for the whole-cell configuration; for CaMKII α -positive neurons, 29.2% for obtaining gigaohm seals and 20.0% for the whole-cell configuration) are comparable to or higher than that obtained by manually performing two-photon image-guided patching of fluorescently labeled neurons *in vivo* (for us, 10.6% success rate for manual whole-cell patching of tdTomato-expressing PV-positive

Figure 3. Imagepatcher Operation

- (A) Two-photon images of a parvalbumin (PV)-positive neuron acquired at three different time points (indicated by Roman numerals for reference in B and C) during closed-loop real-time image-guided pipette positioning. White, sketch of pipette tip; green, Alexa 488; red, tdTomato; x, target cell centroid; numbers in the upper right, vector (x, y, z) from the pipette tip to the target cell centroid (in μm).
- (B) Pipette current traces in response to 10 mV voltage pulses, with Roman numerals indicating the corresponding images in (A).
- (C) Pipette resistance during imagepatching over time, with Roman numerals corresponding to time points referenced in (A) and (B): (Ci) pipette is 12 μm above the target cell centroid, (Cii) pipette is 6 μm above the centroid, (Ciii) pipette is 0 μm above the centroid (i.e., in contact with the cell), (Civ) gigaohm seal is established, and (Cv) cell is broken into.
- (D) Maximum intensity projection (MIP) of a z stack (48 images, 2 μm step size) of an imagepatched PV-positive neuron, showing tdTomato (left, red), Alexa 488 (middle, green), and overlay (right).

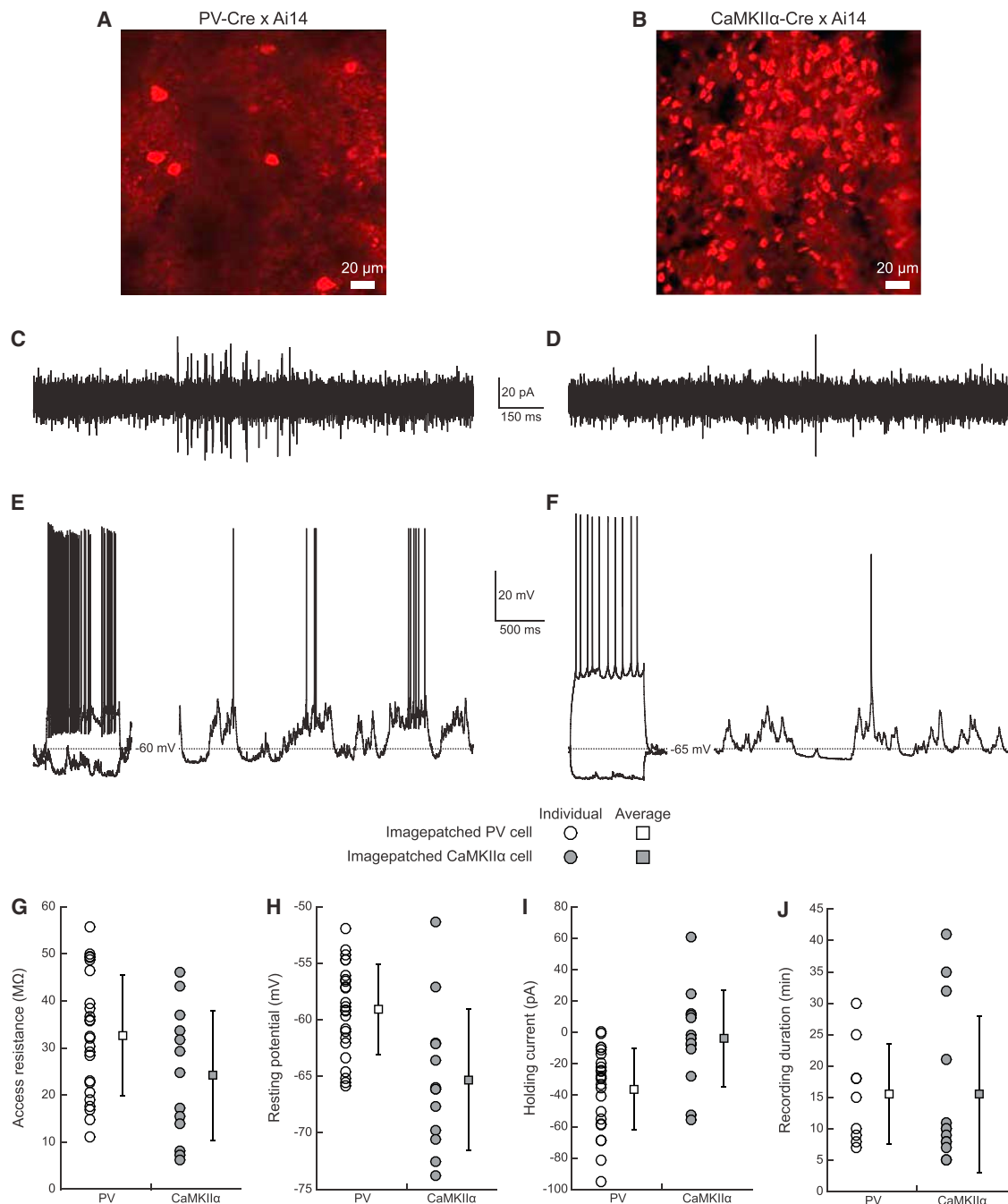


Figure 4. Imagepatching of Multiple Cell Types in Mouse Cortex

(A) Maximum intensity projection of a z stack (20 images, 5 μ m step size) of tdTomato (red)-expressing PV-positive cells in layer 2/3 somatosensory cortex of a PV-Cre x Ai14 mouse.

(B) Maximum intensity projection of a z stack (20 images, 5 μ m step size) of tdTomato (red)-expressing CaMKII α -positive cells in layer 2/3 somatosensory cortex of a CaMKII α -Cre x Ai14 mouse.

(C) Cell-attached current recording from an imagepatched PV-positive neuron.

(D) Cell-attached current recording from an imagepatched CaMKII α -positive neuron.

(E) Whole-cell voltage recordings from an imagepatched PV-positive neuron under current injection (left, -100 and $+200$ pA), and at rest (right).

(F) Whole-cell voltage recordings from an imagepatched CaMKII α -positive neuron under current injection (left, -100 and $+200$ pA), and at rest (right).

(G–J) Recording quality of imagepatched PV-positive neurons (white symbols; $n = 24$ cells from 14 PV-Cre x Ai14 mice for G–I; $n = 9$ cells from five PV-Cre x Ai14 mice for J) and imagepatched CaMKII α -positive neurons (gray symbols; $n = 13$ cells from seven CaMKII α -Cre x Ai14 mice) in somatosensory and motor cortices of isoflurane-anesthetized mice. Square and error bars are mean \pm SD.

(legend continued on next page)

neurons; $n = 11$ out of 104 attempts, 19 PV-Cre x Ai14 mice; a 10%–20% success rate for obtaining a whole-cell recording from an EGFP-labeled PV-positive neuron was reported in [Margrie et al., 2003](#)). During our imagepatching experiments, some pipettes were occluded after brain penetration ($n = 22$ out of 108 when targeting PV-positive neurons; 14 out of 65 when targeting CaMKII α -positive neurons; detailed breakdown of unsuccessful patching attempts in [Table S1](#)) and were automatically retracted by the imagepatcher; focusing on trials that entered the closed-loop stage ([Figure 1Biv](#)), the rates of successfully achieving the gigaohm seal and the whole-cell configuration were 48.8% and 27.9%, respectively ($n = 42$ gigaohm seals and 24 whole-cell configurations out of 86 trials) for PV-positive neurons and 37.3% and 25.5%, respectively ($n = 19$ gigaohm seals and 13 whole-cell configurations out of 51 trials), for CaMKII α -positive neurons. These success rates did not vary substantially with target cell depth ([Table S2](#)), nor with the density of labeled cells around a target cell ([Table S3](#)), suggesting that the imagepatcher performance was consistent.

DISCUSSION

We developed an algorithm and a robotic system that fully automates targeted patch clamping of visually identified cells *in vivo*, by implementing closed-loop real-time imaging to dynamically adjust the pipette position to hone in on a cell of interest. Our strategy makes the imagepatcher the first system that enables fully hands-free navigation of a patch pipette to a targeted cell and subsequent automated patch clamping in the intact brain. Unlike other previous systems that heavily rely on human intervention for successful patch-clamp recordings of visually identified cells ([Long et al., 2015](#); [Perin and Markram, 2013](#); [Steinmeyer and Yanik, 2012](#); [Wu et al., 2016](#)), the imagepatcher eliminates the need for manual adjustments and corrections during the entire patching process, making the robot a powerful tool that can facilitate systematic electrophysiological characterizations of specific classes of cells. Certain factors that can prevent investigators performing manual patching from achieving the whole-cell patch-clamp state, such as variations in pipette trajectory, pipette movement speed, and pipette pressure levels, are also reduced in our automated system. The reduction of variation in these factors provides consistency in patch-clamping procedures that may be difficult to obtain manually and may prove particularly beneficial for studies targeting very sparse populations of cells.

With our software designed to work in parallel with ScanImage operation, and our hardware designed to augment a conventional two-photon microscope in a modular way, the imagepatcher may be adapted to work on any microscope that ScanImage (or another openly modifiable software package) supports. Although our current study focused on targeted patching guided by two-photon microscopy in the intact brain, the

imagepatcher could, in principle, also be used to automate and enable experiments utilizing other imaging modalities (e.g., one-photon fluorescence microscopy) and/or other tissues or preparations—as long as a target provides fluorescence corresponding to its size and position. In the case of experiments involving targeted patching of non-fluorescent, unlabeled cells (i.e., “shadowpatching” developed by [Kitamura et al., 2008](#)), the cell position detection algorithm ([Figure 2B](#)), as it currently stands, may lead to incorrect identification of the target cell’s z-coordinate, because we found from our shadow images that the mean pixel intensity of the cell body shadow does not vary with a defined pattern as a function of microscope focus (unlike cells labeled with a photostable fluorescent marker, which look the brightest when in focus). A new cell position detection algorithm that identifies the z-coordinate of a target cell based on its other properties (e.g., cell body size, cell body shape) might permit, in the future, automation of shadowpatching. The open nature of the imagepatcher code allows for integration of such an algorithm, in addition to tuning of software settings that might be required for different microscopes and imaging conditions.

Integrating our robot with patch pipette cleaning protocols for repeated patch pipette use ([Kolb et al., 2016](#)) may enable the elimination of some of the manual preparatory steps required to utilize imagepatching (e.g., filling a patch pipette with intracellular solution and inserting it into a pipette holder). By developing and using a bright pipette dye that has a fluorescence emission spectrum overlapping minimally (or, ideally, not overlapping at all) with that of the target cells’ fluorescent marker, the high level of background fluorescence that results from multiple penetrations into the brain may have little or no effect on cell position detection and targeting by the imagepatcher, enabling many imagepatching trials and thus many patch-clamp recordings per animal. Further augmentation of the imagepatcher hardware (i.e., integration of multiple autopatcher control boxes, each linked to an individual pipette, with a single two-photon microscope) and refinement of the software (e.g., code development for simultaneous micromanipulator control in response to multiple pipette impedances and imaged positions of target neurons) may also enable multi-cell targeted patch-clamp recordings *in vivo* ([Jouhannau et al., 2015](#); [Pala and Petersen, 2015](#); [van Welie et al., 2016](#)), which will provide information on how cells communicate with each other in an intact brain network. Although we have not obtained patch-clamp recordings in the awake brain using the imagepatcher, with an appropriate restraint habituation strategy (to reduce brain motion), a robust image analysis approach (which compensates for large motion artifacts), or a strategy for real-time switching of target cell identity (which enables targeting of an alternative cell, if present, when motion artifacts are large enough to displace the originally targeted cell out of the field-of-view), the imagepatcher may enable patch clamping of targeted neurons in awake animals.

(G) Access resistance.
(H) Resting potential.
(I) Holding current.
(J) Recording duration.

STAR★METHODS

Detailed methods are provided in the online version of this paper and include the following:

- **KEY RESOURCES TABLE**
- **CONTACT FOR REAGENT AND RESOURCE SHARING**
- **EXPERIMENTAL MODEL AND SUBJECT DETAILS**
- **METHOD DETAILS**
 - Surgical procedures
 - Electrophysiology
 - Hardware and software setup
 - Assessment of target cell movements in response to pipette navigations into and inside the brain
 - Details of the pipette tip detection algorithm
 - Details of the cell position detection algorithm
 - Micromanipulator-microscope platform calibration
 - Details of the imagepatcher operation
 - Performance of the pipette tip detection algorithm at angles other than 30° below the horizontal
 - Derivation of pipette pressure for brain entry and cell approach
 - Optimization of cell-pipette contact detection, gigaseal formation, and break-in
 - Derivation of dye-ejection based pipette blockage test
 - Quantification of PV-positive and CaMKII α -positive cell densities
 - Input resistance and spontaneous firing rates of image-patched cells
- **QUANTIFICATION AND STATISTICAL ANALYSIS**
- **DATA AND SOFTWARE AVAILABILITY**

SUPPLEMENTAL INFORMATION

Supplemental Information includes four figures, three tables, and Methods S1 and can be found with this article at <http://dx.doi.org/10.1016/j.neuron.2017.08.011>.

AUTHOR CONTRIBUTIONS

H.-J.S., I.v.W., S.B.K., C.R.F., and E.S.B. conceived strategies for automating image-guided patch-clamp recordings *in vivo*. H.-J.S. and I.v.W. conducted experiments, analyzed data, and conceived the imagepatching algorithm. H.-J.S. wrote the MATLAB program for the imagepatcher. B.A. assisted with experiments and optimization of portions of the imagepatching algorithm. E.S.B. supervised the project. H.-J.S., I.v.W., and E.S.B. wrote the paper, with input from all authors.

ACKNOWLEDGMENTS

We thank S. Komai (Nara Institute of Science and Technology, Japan), L. Gentet (Lyon Neuroscience Research Center, France), A. Pala (Georgia Tech, USA), and I.-W. Chen (Université René Descartes, France) for advice and information on manual two-photon image-guided patch-clamp recordings *in vivo*. We would also like to acknowledge D. Park (MIT, USA) for assistance with manual image-guided patch-clamp recordings in acute brain slices. We thank L.-H. Tsai and C. Adaikkan (MIT, USA) for supplying CaMKII α -Cre x Ai14 mice. We thank T. Diefenbach (Harvard University, USA) for advice and information on the Ultima IV two-photon microscope, and C. Deister (Brown University, USA) as well as C. Sun (MIT, USA) for assistance with operating the Ultima IV two-photon microscope with ScanImage 3.8. We also thank I. Wickersham (MIT, USA) for advice on the autopatcher control box assembly. H.-J.S. ac-

knowledges the Samsung Scholarship. E.S.B. acknowledges support by Jeremy and Joyce Wertheimer, NIH 1R01NS102727, NIH 1R01EY023173, NIH 1R01MH103910, NIH Director's Pioneer Award 1DP1NS087724, the MIT Synthetic Intelligence Project, the MIT Media Lab, the HHMI-Simons Faculty Scholars Program, and the New York Stem Cell Foundation–Robertson Award. All of the authors on the paper are inventors on a patent application describing this invention.

Received: January 23, 2017

Revised: June 27, 2017

Accepted: August 4, 2017

Published: August 30, 2017; corrected online September 20, 2017

REFERENCES

- Altamura, C., Dell'Acqua, M.L., Moessner, R., Murphy, D.L., Lesch, K.P., and Persico, A.M. (2007). Altered neocortical cell density and layer thickness in serotonin transporter knockout mice: a quantitation study. *Cereb. Cortex* *17*, 1394–1401.
- Atallah, B.V., Bruns, W., Carandini, M., and Scanziani, M. (2012). Parvalbumin-expressing interneurons linearly transform cortical responses to visual stimuli. *Neuron* *73*, 159–170.
- Chen, I.-W., Helmchen, F., and Lütcke, H. (2015). Specific early and late oddball-evoked responses in excitatory and inhibitory neurons of mouse auditory cortex. *J. Neurosci.* *35*, 12560–12573.
- Clarke, S.D. (1993). Regulation of fatty acid synthase gene expression: an approach for reducing fat accumulation. *J. Anim. Sci.* *77*, 1957–1965.
- Dittgen, T., Nimmerjahn, A., Komai, S., Licznanski, P., Waters, J., Margrie, T.W., Helmchen, F., Denk, W., Brecht, M., and Osten, P. (2004). Lentivirus-based genetic manipulations of cortical neurons and their optical and electrophysiological monitoring *in vivo*. *Proc. Natl. Acad. Sci. USA* *101*, 18206–18211.
- Gentet, L.J., Avermann, M., Matyas, F., Staiger, J.F., and Petersen, C.C.H. (2010). Membrane potential dynamics of GABAergic neurons in the barrel cortex of behaving mice. *Neuron* *65*, 422–435.
- Gentet, L.J., Kremer, Y., Taniguchi, H., Huang, Z.J., Staiger, J.F., and Petersen, C.C. (2012). Unique functional properties of somatostatin-expressing GABAergic neurons in mouse barrel cortex. *Nat. Neurosci.* *15*, 607–612.
- Häusser, M., and Margrie, T.W. (2014). Two-photon targeted patching and electroporation *in vivo*. *Cold Spring Harb. Protoc.* *2014*, 78–85.
- Hippenmeyer, S., Vrieseling, E., Sigrist, M., Portmann, T., Laengle, C., Ladle, D.R., and Arber, S. (2005). A developmental switch in the response of DRG neurons to ETS transcription factor signaling. *PLoS Biol.* *3*, 0878–0890.
- Jouhanneau, J.-S., Kremkow, J., Dorm, A.L., and Poulet, J.F.A. (2015). *In vivo* monosynaptic excitatory transmission between layer 2 cortical pyramidal neurons. *Cell Rep.* *13*, 2098–2106.
- Kitamura, K., Judkewitz, B., Kano, M., Denk, W., and Häusser, M. (2008). Targeted patch-clamp recordings and single-cell electroporation of unlabeled neurons *in vivo*. *Nat. Methods* *5*, 61–67.
- Kodandaramaiah, S.B., Franzesi, G.T., Chow, B.Y., Boyden, E.S., and Forest, C.R. (2012). Automated whole-cell patch-clamp electrophysiology of neurons *in vivo*. *Nat. Methods* *9*, 585–587.
- Kodandaramaiah, S.B., Holst, G.L., Wickersham, I.R., Singer, A.C., Franzesi, G.T., McKinnon, M.L., Forest, C.R., and Boyden, E.S. (2016). Assembly and operation of the autopatcher for automated intracellular neural recording *in vivo*. *Nat. Protoc.* *11*, 634–654.
- Kolb, I., Stoy, W.A., Rousseau, E.B., Moody, O.A., Jenkins, A., and Forest, C.R. (2016). Cleaning patch-clamp pipettes for immediate reuse. *Sci. Rep.* *6*, 35001.
- Komai, S., Denk, W., Osten, P., Brecht, M., and Margrie, T.W. (2006). Two-photon targeted patching (TPTP) *in vivo*. *Nat. Protoc.* *1*, 647–652.
- Lee, A.K., Epszstein, J., and Brecht, M. (2009). Head-anchored whole-cell recordings in freely moving rats. *Nat. Protoc.* *4*, 385–392.

- Li, L.Y., Xiong, X.R., Ibrahim, L.A., Yuan, W., Tao, H.W., and Zhang, L.I. (2015). Differential receptive field properties of parvalbumin and somatostatin inhibitory neurons in mouse auditory cortex. *Cereb. Cortex* 25, 1782–1791.
- Long, B., Li, L., Knoblich, U., Zeng, H., and Peng, H. (2015). 3D image-guided automatic pipette positioning for single cell experiments in vivo. *Sci. Rep.* 5, 18426.
- Margrie, T.W., Brecht, M., and Sakmann, B. (2002). In vivo, low-resistance, whole-cell recordings from neurons in the anaesthetized and awake mammalian brain. *Pflügers Arch.* 444, 491–498.
- Margrie, T.W., Meyer, A.H., Caputi, A., Monyer, H., Hasan, M.T., Schaefer, A.T., Denk, W., and Brecht, M. (2003). Targeted whole-cell recordings in the mammalian brain in vivo. *Neuron* 39, 911–918.
- Mateo, C., Avermann, M., Gentet, L.J., Zhang, F., Deisseroth, K., and Petersen, C.C.H. (2011). In vivo optogenetic stimulation of neocortical excitatory neurons drives brain-state-dependent inhibition. *Curr. Biol.* 21, 1593–1602.
- Mountcastle, V.B. (2003). Introduction. *Computation in cortical columns. Cereb. Cortex* 13, 2–4.
- Pala, A., and Petersen, C.C.H. (2015). In vivo measurement of cell-type-specific synaptic connectivity and synaptic transmission in layer 2/3 mouse barrel cortex. *Neuron* 85, 68–75.
- Perin, R., and Markram, H. (2013). A computer-assisted multi-electrode patch-clamp system. *J. Vis. Exp.* <http://dx.doi.org/10.3791/50630>.
- Pologruto, T.A., Sabatini, B.L., and Svoboda, K. (2003). ScanImage: flexible software for operating laser scanning microscopes. *Biomed. Eng. Online* 2, 13.
- Runyan, C.A., Schummers, J., Van Wart, A., Kuhlman, S.J., Wilson, N.R., Huang, Z.J., and Sur, M. (2010). Response features of parvalbumin-expressing interneurons suggest precise roles for subtypes of inhibition in visual cortex. *Neuron* 67, 847–857.
- Steinmeyer, J.D., and Yanik, M.F. (2012). High-throughput single-cell manipulation in brain tissue. *PLoS ONE* 7, e35603.
- Tsien, J.Z., Chen, D.F., Gerber, D., Tom, C., Mercer, E.H., Anderson, D.J., Mayford, M., Kandel, E.R., and Tonegawa, S. (1996). Subregion- and cell type-restricted gene knockout in mouse brain. *Cell* 87, 1317–1326.
- van Welie, I., Roth, A., Ho, S.S.N., Komai, S., and Häusser, M. (2016). Conditional spike transmission mediated by electrical coupling ensures millisecond precision-correlated activity among interneurons in vivo. *Neuron* 90, 810–823.
- Wilson, N.R., Schummers, J., Runyan, C.A., Yan, S.X., Chen, R.E., Deng, Y., and Sur, M. (2013). Two-way communication with neural networks in vivo using focused light. *Nat. Protoc.* 8, 1184–1203.
- Wu, Q., Kolb, I., Callahan, B.M., Su, Z., Stoy, W., Kodandaramaiah, S.B., Neve, R., Zeng, H., Boyden, E.S., Forest, C.R., and Chubykin, A.A. (2016). Integration of autpatching with automated pipette and cell detection in vitro. *J. Neurophysiol.* 116, 1564–1578.

STAR★METHODS

KEY RESOURCES TABLE

REAGENT or RESOURCE	SOURCE	IDENTIFIER
Software and Algorithms		
ScanImage	Pologruto et al., 2003	http://scanimage.vidriotechnologies.com/display/SlH/ScanImage
Imagepatcher code	This paper	Included as Methods S1
Other		
Code, schematics, and parts lists for the imagepatcher	This paper	http://autopatcher.org

CONTACT FOR REAGENT AND RESOURCE SHARING

All code, schematics, and parts lists will also be posted to <http://autopatcher.org> at time of publication. Further requests and inquiries should be directed to, for fulfillment by, the Lead Contact, Dr. Edward S Boyden (esb@media.mit.edu).

EXPERIMENTAL MODEL AND SUBJECT DETAILS

All experimental procedures were performed on 6 – 8 week old transgenic mice, male and female used equally, of PV-Cre (Jax strain #: 017320) x Ai14 (tdTomato; Jax strain #: 007914) genotype or CaMKII α -Cre (Jax strain #: 005359) x Ai14 (tdTomato; Jax strain #: 007914) genotype, in accordance with protocols approved by the Massachusetts Institute of Technology (MIT) Committee on Animal Care (CAC). Six PV-Cre x Ai14 mice were used to quantify neuron movements in response to a pipette entering the brain ([Figure S1A](#)), and seventeen additional PV-Cre x Ai14 mice were used to measure how much neurons change their locations when a pipette is navigated toward them inside the brain ([Figure S1B](#)). Eight PV-Cre x Ai14 mice were used to find the set of optimal pipette pressure levels for brain entry and cell approach during patching (see [STAR Methods](#), “Derivation of pipette pressure for brain entry and cell approach”). Z stacks of tdTomato-labeled parvalbumin (PV)-positive neurons, which were used to validate our cell detection algorithm ([Figure 2B](#)), were obtained from somatosensory and motor cortices of five PV-Cre x Ai14 mice. We used twenty PV-Cre x Ai14 mice to optimize the portion of the closed-loop image-guided pipette positioning stage responsible for resistance-based detection of the pipette tip-cell membrane contact, as well as the gigaseal formation and the break-in stages (see [STAR Methods](#), “Optimization of cell-pipette contact detection, gigaseal formation, and break-in”). Three PV-Cre x Ai14 mice were used to derive the dye-based pipette blockage test (see [STAR Methods](#), “Derivation of dye-ejection based pipette blockage test”). For comparing the cortical density of calcium/calmodulin-dependent protein kinase II alpha (CaMKII α)-positive neurons to that of PV-positive neurons, z stacks of tdTomato-expressing cells were obtained from somatosensory and motor cortices of seven CaMKII α -Cre x Ai14 mice and nine PV-Cre x Ai14 mice. To validate the robotic system running the imagepatching algorithm ([Figure 4](#)), seventeen PV-Cre x Ai14 mice and ten CaMKII α -Cre x Ai14 mice were used, while nineteen PV-Cre x Ai14 mice were used for the manual patching experiments ([Figures S4A–S4C](#)).

METHOD DETAILS

Surgical procedures

Throughout the surgery, mice were anesthetized with 1 – 2% (vol/vol) isoflurane in oxygen and maintained at 37°C using a heating pad. After shaving the scalp, the mouse was placed in a custom-built stereotax, with its eyes covered with ophthalmic ointment. Betadine and 70% ethanol were then applied to the shaved area for sterilization. A polycarbonate recording chamber was implanted on the skull using dental acrylic, and a 1 – 2 mm diameter craniotomy, contained inside a 3 mm diameter window of the recording chamber, was made 1.5 – 2 mm posterior to bregma and 1.5 – 2 mm to the right of the midline. The dura was then carefully removed to expose the brain surface. Right before starting an imaging or a patch-clamp experiment, 1.5% (vol/w) agar in HEPES buffered artificial cerebrospinal fluid (ACSF, containing 145 mM NaCl, 5.4 mM KCl, 10 mM HEPES, 1.8 mM CaCl₂, 1 mM MgCl₂ ([Chen et al., 2015](#)) or 150 mM NaCl, 2.5 mM KCl, 10 mM HEPES, 2 mM CaCl₂ and 1 mM MgCl₂ ([van Welie et al., 2016](#)); pH adjusted to 7.3 – 7.4 with NaOH) was applied on top of the brain to dampen pulsations caused by respiration and heartbeat, and then the craniotomy was covered with ACSF to keep the brain moist throughout the experiment. We took extra care to minimize bleeding throughout the surgery as blood on the cortical surface can greatly diminish optical clarity during two-photon imaging ([Komai et al., 2006](#)). In case of bleeding, the brain surface was irrigated with ACSF to stop the bleeding and remove as much blood as possible from the cortical surface. At the end of the experiment, mice were euthanized under anesthesia.

Electrophysiology

Cell-attached and whole-cell patch-clamp recordings were performed on mice under 1 – 1.5% isoflurane anesthesia on a 37°C heating pad (DC Temperature Control System, FHC). Patch pipettes with resistance values between 5 – 7.5 M Ω were prepared by pulling filamented borosilicate glass capillaries (Warner or WPI) using a micropipette puller (Flaming-Brown P97 model, Sutter Instruments or PC-10 vertical puller, Narishige). These pipettes were filled with an internal solution containing (in mM): 135 K-gluconate, 4 KCl, 10 HEPES, 10 Na₂-phosphocreatine, 4 MgATP, 0.3 Na₃GTP (pH adjusted to 7.3 – 7.4 with KOH; osmolarity 280 – 290 mOsm), and 50 μ M Alexa 488 dye (ThermoFisher; for pipette visualization under the two-photon microscope) or 125 K-Methanesulfonate, 7 KCl, 10 HEPES, 2 MgATP, 2 Na₂ATP, 0.5 Na₂GTP, 0.05 EGTA (pH adjusted to 7.3 with KOH; osmolarity 280–290 mOsm), and 50 μ M Alexa 488 dye. Fully manual patch clamp experiments (Figures S4A–S4C) were performed following previously reported protocols (Häusser and Margrie, 2014; Komai et al., 2006).

Hardware and software setup

We modified a standard two-photon image-guided *in vivo* patch-clamp rig to construct the imagepatching system (Figure 1C). Hardware for the standard rig included a two-photon laser scanning microscope (Ultima moving IV, Prairie Technologies), a mode-locked Ti-sapphire laser (Mai Tai HP; Spectra-Physics), a water-immersion objective (CFI75 LWD 16x W NA 0.8 WD 3.0mm objective, Nikon), a programmable 4-axis micromanipulator comprised of a single-axis micromanipulator (SMX-SA, Sensapex) mounted at a 30° angle below the horizontal on a left-handed three-axis micromanipulator (SMX-L-RS-50-HL-US, Sensapex), a pipette holder (Warner) mounted on the single-axis micromanipulator and connected to the CV-7B headstage of a patch amplifier (Multiclamp 700B, Molecular Devices) via an intermediate cable (IM-SMB, Sensapex), and a digitizer (Digidata 1440A, Molecular Devices) relaying signals between the amplifier and a computer. The laser was set to emit 960 nm (~900 mW average output power), which could excite both tdTomato and Alexa 488. To minimize bleed-through, we replaced the user-exchangeable PMT filters in the Ultima (which are optimized for dual labeling using Alexa 594 and Alexa 488) with red (630/30 nm, Chroma) and green (510/10 nm, Semrock) filters. The 4-axis micromanipulator was connected to a rotary knob controller (SMXS-K-2-RS-US) that communicated with the computer through a USB port.

The patch amplifier and the digitizer of the standard rig were connected to our autopatcher control box as previously described (Kodandaramaiah et al., 2012, 2016) (Figure 1C). The autopatcher control box was constructed as previously described (Kodandaramaiah et al., 2012, 2016), with a slight modification; potentiometers mounted on the front panel of the original autopatcher control box, each of which is used to manually pre-set a pressure value to be used during the autopatcher operation (see Kodandaramaiah et al., 2016 for details), were replaced by analog outputs from a standard data acquisition (DAQ) device (PCIe-6343, National Instruments) that can be programmed to send a command voltage of an arbitrary value to electronic pressure regulators inside the autopatcher control box, thus enabling automated, real-time control of the pipette pressure to any desired level at any rate (e.g., in a ramp) during imagepatcher operation (note that the PCIe-6343 can be replaced by any programmable device that can generate analog outputs ranging from 0 to 5 VDC, and up to 400 mA).

To operate the microscope with ScanImage 3.8, a MATLAB-based open-source software package, previously reported instructions (Wilson et al., 2013) were followed to make necessary connections between the microscope hardware and the computer. ScanImage was configured such that each acquired image has a single frame with 256 lines per frame and 256 pixels per line, and each line is scanned in 2.64 ms for a frame rate of 1.48 frames per second. To acquire high quality images of a neuron at the end of the imagepatching experiment (example image in Figure 3D), ScanImage was configured to produce 2048 lines per frame and 2048 pixels per line at a frame rate of 0.18 frames per second.

We used MATLAB R2013b (MathWorks) to write and run our program executing the imagepatching algorithm. Our program was divided into two main modules: (i) a graphical user interface (GUI) that allows the user to start the imagepatching algorithm and to view the results of image acquisition as well as analysis during the algorithm execution (see Methods S1, “find_cells_gui_S1.m”); (ii) image analysis code that is executed upon the completion of image acquisition to perform real-time image analysis (see Methods S1, “image_autopatcher_v1.m”); MATLAB scripts can be bound to one or more ScanImage events, such as the start of the ScanImage software and the completion of image acquisition, by adding them as user functions; see Methods S1, “Imagepatcher User Manual.docx” and the ScanImage website [<https://openwiki.janelia.org/wiki/pages/viewpage.action?pageId=29524376>] for details). A ScanImage function responsible for image frame generation, called makeFrameByStripes, was augmented with our code to direct raw image data acquired by the microscope to our image analysis code (see Methods S1, “makeFrameByStripes.m,” for the function with our code).

During imagepatcher operation, when the pipette resistance had to be measured, the autopatcher digital board (USB-6211, National Instruments) was used to apply 50 Hz, 10 mV square waves to the pipette tip and to record the resulting current pulses at 20 kHz. 10 mV (i.e., the amplitude of the applied voltage) was divided by the amplitude of each current pulse, and the average of the resulting values was assigned as the pipette resistance while the standard deviation of the resulting values was used as a metric quantifying the amount of heartbeat modulation. We performed whole-cell recordings of patched cells using Clampex 10.4 (Molecular Devices), acquiring data through a low-pass filter (Bessel filter, 10 kHz cutoff) at a rate of 40,000 samples per second. The acquired signals were analyzed using MATLAB 2013b (MathWorks) and Clampfit 10.5 (Molecular Devices).

Assessment of target cell movements in response to pipette navigations into and inside the brain

Cell movements following the pipette navigation into the brain (Figure S1A) were observed by first locating a tdTomato-labeled cell $\sim 150 - 250 \mu\text{m}$ below the brain surface and recording the coordinates of the cell centroid (visually assessed). Using trigonometric functions in MATLAB, the pipette trajectory parallel to the pipette axis (i.e., 30° below the horizontal) was then calculated, setting the start and the end of the trajectory to the locations $25 \mu\text{m}$ above the brain surface and $50 \mu\text{m}$ directly above the cell centroid respectively. Subsequently, a patch pipette whose resistance value was between $5 - 7.5 \text{ M}\Omega$ was filled with internal solution and installed into the pipette holder that was positioned on the left side of the craniotomy. While applying low positive pressure ($\sim 15 - 30 \text{ mBar}$), the pipette was moved into the ACSF covering the brain, positioning the pipette tip at the start position of the calculated trajectory. A high positive pressure ($\sim 200 - 300 \text{ mBar}$) was then applied to the pipette, and the single-axis micromanipulator (i.e., the micromanipulator whose axis is parallel to the pipette axis) was controlled using MATLAB code (Methods S1, “move_sensapex_manipulator_HJS.m”) interacting with a software development kit from Sensapex (the software development kit available on the Sensapex website [<http://www.sensapex.com/support/downloads-updates/>]) to automatically and accurately move the pipette along the calculated trajectory at $\sim 600 \mu\text{m/s}$. When the pipette movement was complete, a z stack (20 or 24 images, $2 \mu\text{m}$ or $3 \mu\text{m}$ step size, 17x zoom) was acquired around the original cell centroid coordinates that were recorded before the pipette movement. The z stack was analyzed post hoc to determine the new coordinates of the cell centroid (visually assessed), and these coordinates were compared to those of the cell centroid before the pipette movement into the brain to quantify the amount of cell displacement.

To determine the amount of cell movement in response to the pipette navigation inside the brain (Figure S1B), a patch pipette (resistance value $5 - 7.5 \text{ M}\Omega$) filled with the internal solution was first placed inside the brain, with its tip located $\sim 20 - 30 \mu\text{m}$ above a tdTomato-labeled cell and $\sim 5 - 13 \mu\text{m}$ away from the cell centroid in the transverse plane, simulating an offset from the pipette tip to the target cell that can result from the pipette entry into the brain. After recording the coordinates of the cell centroid (visually assessed), the micromanipulator was automatically moved using MATLAB code (Methods S1, “move_sensapex_manipulator_HJS.m”) in the x, y, and z directions to place the pipette tip $\sim 10 - 20 \mu\text{m}$ directly above the cell centroid, which is where an investigator manually performing patching would aim to bring the pipette tip to approach the targeted cell in the vertical direction (Häusser and Margrie, 2014; Komai et al., 2006). Once the micromanipulator movement was complete, a z stack (20 or 24 images, $2 \mu\text{m}$ or $3 \mu\text{m}$ step size, 17x zoom) was acquired around the cell centroid coordinates that were recorded prior to the pipette navigation. Post hoc analysis of the z stack was then performed to locate the new cell centroid (visually assessed), coordinates of which were compared to those of the cell centroid before the pipette navigation inside the brain to quantify the amount of cell movement.

Details of the pipette tip detection algorithm

The pipette tip detection algorithm first applies a 2D Gaussian filter (19×19 window; $9/2$ variance) to each image in the z stack of a patch pipette to remove the background noise. The filtered topmost image of the stack is then subjected to a range of threshold values (corresponding to $1 - 95\%$ of the maximum pixel intensity of the filtered image) to determine the maximum threshold value at which the resulting cluster of bright pixels (Figure 2Aii.i, area bounded by yellow outline) has a characteristic shape (i.e., has 3 endpoints when subjected to the bwmorph function with ‘endpoints’ operation in MATLAB); in case of multiple clusters for a single threshold value, the largest cluster (i.e., the cluster composed of the highest number of pixels) is analyzed for the endpoint detection. Subsequently, the cluster obtained from the filtered topmost image at this threshold value is analyzed to determine its area (i.e., number of pixels in the cluster; using MATLAB’s bwboundaries function) and centroid (Figure 2Aii.i, black x; using MATLAB’s regionprops function with ‘centroid’ as an input argument). The detected centroid is also considered as the pixel corresponding to the far end of the pipette (i.e., the end opposite to the pipette tip) and used as the reference point in the subsequent stages of the algorithm. The rest of the filtered images in the stack are then subjected to a range of threshold values, identifying the threshold value for each image at which the resulting cluster has an area closest to that obtained from the topmost image (Figures 2Aii.ii and 2Aii.iii, areas bounded by yellow outlines); in case of multiple clusters for a single threshold value, the largest cluster (i.e., the cluster composed of the highest number of pixels) is used for the area comparison. Each of the resulting clusters is subsequently subjected to MATLAB’s regionprops function (with ‘centroid’ as an input argument) to locate its centroid (Figures 2Aii.ii and 2Aii.iii, yellow x’s). The distance between this cluster centroid and the reference point (i.e., cluster centroid in the topmost image of the stack; Figure 2Aii.i, black x) is calculated for each image, and the calculated values are sorted according to the image number (Figure 2Aiii), with the images in the stack numbered from top to bottom (i.e., the topmost image was image 1). After filtering the sorted distance values with a 5-point moving average filter, the algorithm identifies the image number at which the filtered distance value starts to flatten (Figure 2Aiii, magenta line) by first calculating the approximate derivative of the filtered values (i.e., difference between two consecutive filtered values), then filtering the approximate derivative using a 19-point moving average filter, and finally finding the first instance where the filtered derivative value exceeds the original derivative value. The algorithm assigns the z-coordinate of the corresponding image as the z-coordinate of the pipette tip (Figure 2Aiii, z_{pipette}).

After assigning the z-coordinate of the pipette tip, the algorithm calculates the angle between the cluster centroid in image 1 (Figure 2Aii.i, black x) and the cluster centroid in the image at z_{pipette} , which is assigned as the pipette angle in the transverse plane. Subsequently, the image at z_{pipette} , smoothed by a 2D Gaussian filter (19×19 window; $9/2$ variance) (Figure S3Ai), is segmented using a range of threshold values (corresponding to $5 - 75\%$ of the maximum pixel intensity of the filtered image). The algorithm then analyzes the resulting clusters (Figure S3Aii, white) for the endpoint detection (using the bwmorph function with ‘endpoints’ operation in

MATLAB; Figure S3Aii, yellow boxes); in case of multiple clusters for a single threshold value, the largest cluster (i.e., the cluster composed of the highest number of pixels) is analyzed for the endpoint detection. The lowest threshold value at which the resulting cluster has 3 vertices or endpoints (Figure S3Aii.ii, yellow boxes) is considered optimal for isolating the pixels that accurately represent the entire body of the pipette tip, and the corresponding cluster of pixels (Figure S3Aii.ii, white) is further analyzed for the pipette tip detection; other threshold values that are higher or lower than the optimal value result in clusters that have less or more than 3 endpoints, and are not further analyzed (example images of the clusters resulting from a threshold value higher and lower than the optimal value shown in Figure S3Aii.i and S3Aii.iii, respectively, with the yellow boxes representing the endpoints of these clusters). Out of all the pixels in the cluster resulting from the optimal threshold value, the one that is the furthest away from the centroid of the cluster is identified. Its distance to the centroid is then used as the length of a line (Figure S3Aiii, yellow dotted line) pointing in the direction of the pipette angle in the transverse plane (the angle that was determined earlier as described above) and emanating from the cluster centroid (Figure S3Aiii, yellow x). The pixel in the cluster closest to the endpoint of the line is assigned as the tip of the pipette in the transverse plane (Figure S3Aiii, yellow star; Figure 2Aiv, yellow star), and the location of the pixel in the image is assigned as the x and y coordinates of the pipette tip. See “find_one_pipette_HJS.m” and “pipette_tip_detection_HJS.m” in the Methods S1 for MATLAB codes running the algorithm.

Details of the cell position detection algorithm

The cell position detection algorithm begins its operation by subjecting each image in the z stack of a tdTomato-expressing cell to a 2D Wiener filter (3 × 3 window), removing the background noise. Each filtered image (example filtered image shown in Figure S3Bi) is then segmented using a range of threshold values (corresponding to 5 – 95% of the maximum pixel intensity of the filtered image), and the area of (i.e., the number of pixels in) the resulting clusters of pixels (Figure S3Bii, white) is compared to a reference area (i.e., the area of the target cell chosen by the user during the target cell detection and selection stage); in case of multiple clusters for a single threshold value, the cluster whose centroid is the nearest to the image center and whose area is the closest to the reference area is used for the area comparison. The threshold value at which the resulting cluster of pixels has the area closest to the reference area is considered optimal for identifying the pixels accurately representing the target cell soma, and is isolated by the algorithm from other threshold values that lead to clusters of pixels that represent only a small portion of the cell body (example image of such a cluster shown in Figure S3Bii.i) or capture background pixels (example image of such a cluster shown in Figure S3Bii.iii). The cluster obtained by using the optimal threshold value (Figure S3Bii.ii) is then subjected to MATLAB’s `bwboundaries` function to determine the pixels that represent the boundary (Figure S3Bii.ii, red outline; Figure 2Bii, red outline) and the interior (Figure S3Bii.ii, white; Figure 2Bii, area inside the red outline) of the cross-section of the cell body captured by each image in the stack. The centroid of the cluster (Figure S3Biii, red x) is also determined using MATLAB’s `regionprops` function (with ‘centroid’ as an input argument). The algorithm then calculates the mean intensity of pixels representing the interior of the cell body from each image and sorts the calculated values according to the image number, with the images in the stack numbered from top to bottom (i.e., the topmost image was image 1; example plot of the mean pixel intensity as a function of image number shown in Figure 2Biii). The image capturing the cross-section of the cell body with the highest mean pixel intensity (i.e., the brightest cross-section of the cell body; Figure 2Biii, magenta line) is considered to be focused on the centroid of the cell body, and its z-coordinate is assigned as the z-coordinate of the cell centroid (Figure 2Biii, z_{cell}). Subsequently, the x and y coordinates of the cluster centroid in the image at z_{cell} (Figure S3Biii, red x; Figure 2Biv, red x), which is determined along with the pixels representing the boundary and the interior of the cluster as described above, are assigned as the x and y coordinates of the cell centroid. See “soma_contour_detection.m” and “image_autopatcher_v1.m” in Methods S1 for MATLAB codes running the algorithm.

Micromanipulator-microscope platform calibration

Before performing imagepatching experiments, step sizes of motion and axis angles of the micromanipulator were automatically calibrated to those of the motorized platform of the two-photon microscope, which moved the microscope objective relative to the sample to be imaged, using the imagepatcher. In the first stage of calibration, which was performed once upon initial hardware setup, a patch pipette filled with 50 μM Alexa 488 dye (in deionized water) was installed into the pipette holder, and its tip was manually moved to the center of the field-of-view using the rotary knob controller of the 4-axis micromanipulator. The expected angle below the horizontal for each of the 4 micromanipulator axes was then specified by typing in a value in the corresponding text box on the imagepatcher GUI (for our micromanipulator, 30 for diagonal, 0 for x, 0 for y, and 90 for z axis). Subsequently, the calibration of one of the micromanipulator axes was initiated by clicking one of four pushbuttons displayed on the GUI, each button corresponding to the calibration of each of the 4 axes of the micromanipulator. Pressing the pushbutton started the acquisition of a z stack (20 images, 2 μm step size, 17x zoom) around the pipette. The location of the pipette tip was then automatically identified using the pipette tip detection algorithm (Figure 2A), and the imagepatcher program sent a command to the micromanipulator to move the axis being calibrated forward by a pre-set distance (30 μm for the diagonal axis; 25 μm for x, y, and z axes). Following the micromanipulator movement, the microscope objective was moved to the expected pipette tip position; the expected pipette tip position was calculated by first mapping the micromanipulator axis movement to the x, y, and z directional movements of the motorized platform of the microscope, using both the pipette angle in the transverse plane, which was obtained from the z stack using the pipette tip detection algorithm (Figure 2A), and the expected angle below the horizontal of the moved axis (e.g., when a pipette facing dead-right moves along the diagonal axis by 30 μm , the pipette tip moves by $30 \cdot \cos(30^\circ) \cdot \cos(0^\circ) \approx 26 \mu\text{m}$ in the x-direction, $30 \cdot \cos(30^\circ) \cdot \sin(0^\circ) = 0 \mu\text{m}$

in the y-direction, and $30 \cdot \sin(30^\circ) = 15 \mu\text{m}$ in the z-direction), and then adding the mapped values to the original pipette tip location. With the microscope objective at the expected pipette tip position, another z stack (20 images, $2 \mu\text{m}$ step size, 17x zoom) was acquired, and the actual pipette tip location was determined using the pipette tip detection algorithm (Figure 2A). The angle and the distance between the new tip location and the original tip location were then calculated in the angle and distance units of the microscope's motorized platform. Subsequently, the calculated values were assigned to the forward movement of the micromanipulator axis being calibrated. For the backward movement calibration, the program moved the axis of the micromanipulator backward by the pre-set distance ($30 \mu\text{m}$ for the diagonal axis; $25 \mu\text{m}$ for x, y, and z axes) and then detected the resultant pipette tip location. As done for the forward movement calibration, the angle and the distance between the tip locations before and after the backward movement were calculated in the microscope's motorized platform units, and the calculated values were assigned to the backward movement of the micromanipulator axis being calibrated. The forward and backward movement calibrations were then repeated for other pre-set distances ($55, 150, 320, 350, 420,$ and $480 \mu\text{m}$ for the diagonal axis; $150, 325, 400,$ and $460 \mu\text{m}$ for x and y axes; $50, 150, 200,$ and $250 \mu\text{m}$ for the z axis). Once the calibration for the axis was complete, the calibration results were saved into a .m file, which we could load to our program for future imagepatching experiments. Without replacing the patch pipette, each of the rest of the micromanipulator axes was calibrated in the same way as described above.

The second stage of calibration was implemented to account for a variability in the locked position of the pipette, which stemmed from a lever-based locking mechanism of our micromanipulator. Unlike the first stage that was performed only once, the second stage of calibration was automatically executed for each imagepatching experiment at the start of the brain penetration stage (Figure 1Biii). Right before performing the second stage of calibration, the amount that each micromanipulator axis would have to move to reach the targeted position inside the brain (i.e., $50 \mu\text{m}$ directly above the target cell centroid) was calculated using the calibration results from the first stage of calibration. Subsequently, the new calibration results were obtained by moving each micromanipulator axis by the calculated amount and finding the new pipette tip location following the axis movement; the new pipette tip location was determined using the same procedure implemented for the first stage of calibration, except the expected pipette tip position after the micromanipulator movement was calculated using the calibration results from the first stage of calibration instead of the expected angle below the horizontal specified in the imagepatcher GUI. See "find_cells_gui_S1.m" in Methods S1 for MATLAB code executing the calibration.

Details of the imagepatcher operation

At the start of the imagepatching experiment, we opened ScanImage and imaged the brain inside the craniotomy to visually determine the location of the brain surface. The z-position of the objective corresponding to where we found the brain surface was denoted as the z-coordinate of the brain surface by the imagepatcher. We then specified the number of images (5 – 10), the step size between two consecutive images ($5 - 10 \mu\text{m}$), and the starting depth ($100 - 250 \mu\text{m}$) of a z stack to be acquired inside the brain by using the corresponding text boxes on the imagepatcher GUI. The z stack acquisition (and the target cell detection and selection stage; Figure 1Bi) was started by pressing the corresponding pushbutton on the imagepatcher GUI, and a display window inside the GUI sequentially showed the most recently acquired image during the stack acquisition. At the end of the stack acquisition, the GUI also showed the list of acquired images, which could be used to select images to display in the display window and to run automated cell detection on. After choosing 1 – 3 images, each capturing at least one or two bright cells (visually assessed), by clicking the images in the list, we set the minimum brightness (specified as percentage of the maximum pixel intensity of each of the selected images) of cells to detect to any value between 10 and 75% while setting the desired minimum and maximum cell body radii to 3 and $15 \mu\text{m}$ respectively by using the corresponding text boxes on the GUI. Out of all the tdTomato-expressing neurons captured by the images, only those that met our detection criteria were identified by the imagepatcher and shown with red outlines in the display window of the GUI; the imagepatcher detected the cells by smoothing each of the selected images using a 2D Wiener filter (3×3 window), then segmenting each of the filtered images using the minimum brightness as the threshold value, and finally determining the boundary of resulting objects that met our radii specifications (see "find_center_and_circle_soma_cell_radius_range.m" in Methods S1 for MATLAB code responsible for the cell detection). To conclude the target cell detection and selection stage, we chose a target cell to patch by clicking the interior of one of the outlined cells in the display window, which turned the outline of the selected cell to yellow and registered the information about the target cell (x, y coordinates of the target cell centroid, z-coordinate of the target cell depth, area of the target cell, minimum brightness threshold for the cell detection) in the imagepatcher.

Following the target cell selection, we initiated the pipette tip detection stage (Figure 1Bii) by clicking the corresponding pushbutton on the GUI. This stage began with the autopatcher control box outputting 15 mBar to the pipette while the imagepatcher moved the microscope objective vertically to position the objective away from the brain surface and to provide enough space for a patch pipette. We then filled a pipette with the internal solution, installed it into the pipette holder, and used the rotary knob controller of the 4-axis micromanipulator to manually move the pipette tip to the center of the objective field-of-view (FOV). While imaging the pipette via ScanImage, we used a slider presented on the imagepatcher GUI to adjust pipette pressure to a value that minimized a plume of dye at the pipette tip and subsequently made the pipette tip clearly visible (visually assessed; typically 6 to 8 mBar). A z stack (20 images, $2 \mu\text{m}$ step size, 17x zoom) was then acquired around the pipette tip by pressing the corresponding pushbutton on the GUI. From this stack of images, the imagepatcher detected the pipette tip (using the pipette tip detection algorithm described in Figure 2A) and logged the maximum intensity of pixels representing the pipette in the image focused on the pipette tip.

Next, the brain penetration stage (Figure 1Biii) was started by clicking the corresponding pushbutton on the GUI. Before moving the pipette into the brain, step sizes of motion and axis angles of the micromanipulator were automatically calibrated to those of the

motorized platform of the two-photon microscope (i.e., the second stage of micromanipulator calibration was performed; see “Micromanipulator-microscope platform calibration” section for details); in subsequent steps of the imagepatching process, the imagepatcher calculated the pipette tip location by adding calibrated micromanipulator axes displacements to the original pipette tip location. Following the calibration, the imagepatcher calculated a linear path along the diagonal axis of the micromanipulator (i.e., a trajectory parallel to the pipette axis) with the start and end points located 25 μm above the brain surface and 50 μm directly above the target cell centroid respectively. The micromanipulator was then automatically moved to bring the pipette tip to the start point of the calculated path, and 600 mBar was applied to the pipette by the autopatcher control box. At this point, the imagepatcher measured the pipette resistance for 5 s and displayed the result; if the displayed value was outside of an acceptable range (e.g., 5 – 7.5 M Ω), it was assumed that the pipette was clogged with some undesired particles (in case of resistance greater than 7.5 M Ω) or the pipette tip was broken (in case of resistance less than 5 M Ω), and we retracted the pipette to install a new one. For the pipette with a resistance value within the acceptable range, the imagepatcher logged the pipette resistance and then moved the pipette along the calculated path into the brain. Once the pipette tip entered the brain and was positioned 75 μm above the target cell centroid (i.e., 25 μm above the endpoint of the calculated trajectory), dye ejection at the pipette tip was examined by the imagepatcher to check the pipette tip quality; if an image (17x zoom) capturing the pipette tip at the center of its FOV had either the maximum pixel intensity at least 2 times higher than that logged at the end of the pipette tip detection stage (i.e., maximum intensity of pixels representing the pipette in the image focused on the pipette tip, acquired outside the brain), or the median of pixel intensities at least 40% of the maximum pixel intensity of the image and the maximum pixel intensity at least as high as the maximum intensity logged at the end of the pipette tip detection stage, the imagepatcher considered the pipette tip to be clean (see STAR Methods, “Derivation of dye-ejection based pipette blockage test” for derivation of these criteria). Once the clean pipette tip reached the end point of the calculated path (i.e., 50 μm above the target cell centroid), its pressure was automatically lowered to 300 mBar, and the imagepatcher checked the pipette tip for clogging by measuring the pipette resistance and comparing the measured value to the value obtained outside the brain (i.e., 25 μm above the brain surface), and by performing another evaluation of dye ejection. After this quality check, the imagepatcher acquired a z stack (25 images, 3 μm step size, 17x zoom) around the original target cell centroid (i.e., target cell centroid logged at the end of the target cell detection and selection stage) and determined the target cell position (using the cell position detection algorithm described in Figure 2B) to update the target cell location. The imagepatcher then logged this new cell position and moved the x, y, and z axes of the micromanipulator such that the pipette tip would be 25 μm directly above the updated target cell centroid. After the micromanipulator movement, the dye ejection and the pipette resistance were again examined by the imagepatcher to check the pipette tip for clogging, concluding the brain penetration stage.

At the start of the closed-loop real-time image-guided pipette positioning stage (Figure 1Biv), the pipette pressure was automatically lowered to 100 mBar, and another z stack (15 or 25 images, 2 μm step size, 17x zoom; 15 images were obtained if the micromanipulator movement along the z axis at the end of the brain penetration stage was less than 30 microns; 25 images otherwise) was automatically acquired around the target cell centroid logged during the brain penetration stage. After finding the coordinates of the target cell centroid from the stack (using the cell position detection algorithm described in Figure 2B), the imagepatcher entered the closed-loop (Figure 1A), repeatedly updating the cell centroid location and positioning the pipette tip directly above the cell centroid following each 3 μm -pipette step in the z-direction. Every z-step of the pipette was followed by automatic acquisition of two images; to support repeated cell centroid detection while minimizing image acquisition time, one image, instead of a full z stack, was captured at the z-coordinate of the cell centroid determined at the start of the stage, with an assumption that small z-steps used in the closed-loop would cause negligible movement of the cell in the z-direction; the second image was acquired at the calculated location of the pipette tip to check for dye ejection and subsequently verify the pipette tip quality as done in the preceding stage. The imagepatcher also measured the pipette resistance and logged the measured value after each pipette step in the z-direction to monitor changes in the pipette resistance. When the imagepatcher detected a small resistance increase while approaching the target cell, the pipette pressure was automatically lowered to 30 mBar and the current pulses at the pipette tip were checked for another increase in resistance as well as heartbeat modulation, both of which indicated tight contact between the pipette tip and the cell membrane.

Once this resistance increase and heartbeat modulation were detected, the imagepatcher initiated the gigaseal formation stage (Figure 1Bv). In this stage, the pipette movement was stopped, and suction as well as hyperpolarizing voltage were automatically applied to form a gigohm seal between the pipette and the cell membrane. Once a stable gigaseal was established (i.e., the pipette resistance stayed above a gigohm and did not increase by more than 15% over a 15 s period), the imagepatcher GUI displayed a pushbutton for starting the break-in process. By clicking this pushbutton, we started the break-in stage (Figure 1Bvi). If we required cell-attached extracellular recordings, signals from the cell were recorded before initiating the break-in stage (i.e., before clicking the pushbutton). At the start of the break-in stage, the imagepatcher established a baseline of cell filling by the pipette dye (i.e., determined the amount of pipette dye inside the target cell) by acquiring a z stack (10 images, 2 μm step size, 17x zoom) around the cell, identifying pixels corresponding to the cell body in the focused image of the stack using the cell position detection algorithm described in Figure 2B, and calculating the mean pixel intensity of the cell body in the microscope channel corresponding to the pipette dye (channel 2 for our microscope). Subsequently, suction pulses were applied in a ramp by the autopatcher control box while monitoring the seal resistance. Once the resistance dropped below a value characteristic of the whole-cell state, the imagepatcher imaged the target cell again (around the cell depth and centroid determined from the previous z stack; 10 images, 2 micron step size, 17x zoom) to calculate the mean pixel intensity within the cell boundary in channel 2. When the new mean pixel intensity value of the cell body in the focused image of the stack was at least 15% higher than the original value obtained before the suction pulses, the

imagepatcher considered the cell to be filled sufficiently with the pipette dye and concluded the break-in stage. Once the imagepatcher operation was complete, we recorded signals from cells that had achieved a successful whole-cell state, which we defined as that requiring no more than 500 pA current injection to hold the cell at -65 mV (i.e., exhibiting holding current less than or equal to 500 pA) in the voltage-clamp mode, as we did previously (Kodandaramaiah et al., 2012). See Imagepatcher User Manual in [Methods S1](#) for detailed description on how to interact with the imagepatcher GUI for an imagepatching experiment.

Performance of the pipette tip detection algorithm at angles other than 30° below the horizontal

15 pipettes all angled at 25° below the horizontal were each imaged using a z stack ($2\ \mu\text{m}$ step size, 20 images, 17x zoom), with each z stack capturing the pipette tip at a distinct position within the stack. By applying the pipette tip detection algorithm (Figure 2A) to each of the 15 z stacks, we found that the algorithm yielded pipette tip locations that were close to those determined visually, with the tip positions from the algorithm and from visual assessment differing by (mean \pm s.d.) $-1.5 \pm 1.4\ \mu\text{m}$, $0.1 \pm 1.0\ \mu\text{m}$, and $1.6 \pm 3.0\ \mu\text{m}$ in the x, y, and z directions respectively. The pipette tip detection algorithm also enabled accurate tip detection from another 15 z stacks ($2\ \mu\text{m}$ step size, 20 images, 17x zoom) that each captured the tip of a separate pipette angled at 35° below the horizontal at a distinct position within the stack; the tip locations determined by the pipette tip detection algorithm from the 15 z stacks were (mean \pm s.d.) $-0.7 \pm 0.5\ \mu\text{m}$, $-0.5 \pm 0.8\ \mu\text{m}$, and $0.4 \pm 1.4\ \mu\text{m}$ off of the visually assessed tip positions in the x, y, and z directions respectively.

Derivation of pipette pressure for brain entry and cell approach

To determine the optimal pipette pressure for entering the brain during the brain penetration stage (Figure 1Biii), a few penetrations were performed with 100 mBar, 200 mBar, 400 mBar, 600 mBar, and 800 mBar pressure applied at the back of the pipette (these pressure values were chosen based on previously reported protocols for fully manual two-photon image-guided or blind patch-clamp recordings *in vivo* (Häusser and Margrie, 2014; Komai et al., 2006; Lee et al., 2009; Margrie et al., 2002), in which pipette pressure ranging from 100 mBar to 800 mBar were typically used). For our experiments, we used Alexa 488-filled patch pipettes angled at 30° below the horizontal, moving $300 - 400\ \mu\text{m}$ in the diagonal direction (i.e., parallel to the pipette axis), from outside the brain near the brain surface to inside the brain (i.e., $150 - 200\ \mu\text{m}$ deep in the cortex; layer 2/3 for adult mouse brain (Altamura et al., 2007; Mountcastle, 2003)), at $\sim 600\ \mu\text{m}/\text{s}$ (i.e., the maximum speed that our 4-axis micromanipulator could generate under software control). As expected, higher pressure (i.e., 600 mBar and 800 mBar) produced less pipette blockage compared to lower pressure values. However, 800 mBar led to much background signal that caused bleed-through of the Alexa 488 signal into the imaging channel used to visualize tdTomato, making it difficult to resolve tdTomato-expressing cells after brain penetration. As a result, we decided to focus on 600 mBar and found the pressure to cause a reasonably low pipette blockage rate (12.5%; 2 out of 16 trials; 3 PV-Cre x Ai14 mice) when used as the pipette pressure for brain penetration. We therefore chose to implement 600 mBar as the pipette pressure for brain entry during the brain penetration stage of the imagepatching algorithm (Figure 1Biii).

The optimal set of pipette pressure levels for approaching the cell once inside the brain was determined based on our manual patching experiments as well as the values provided in previously reported protocols for manual patching (Häusser and Margrie, 2014; Komai et al., 2006). During our manual slice and *in vivo* patching experiments, we had a few trials in which a gigaohm seal was quickly obtained with an Alexa 488-filled pipette that continuously ejected a plume of dye at its tip until right before it made contact with the target cell. From these trials, we inferred that one of the most critical prerequisites of gigaohm formation might be maintaining a “clean” pipette tip throughout its movement inside the tissue, all the way up to the point where it makes contact with the target cell (this assumption agrees with what has been briefly described in Margrie et al., 2002). During our initial experiments, we observed that the pipette would often cease to eject the dye at its tip (i.e., the pipette was contaminated, as described in Komai et al., 2006) while moving inside the tissue at $20 - 40$ mBar, which is the range of pipette pressure values used in previously reported protocols for two-photon image-guided patching *in vivo* (Häusser and Margrie, 2014; Komai et al., 2006). We tried a few different pressure values that were higher than 40 mBar, and found $100 - 300$ mBar to be high enough to keep the pipette tip blockage rate reasonably low (21.7%; 5 out of 23 trials; 5 PV-Cre x Ai14 mice) while navigating the pipette inside the tissue, but not so high as to cause bleed-through of the pipette dye fluorescence into the tdTomato imaging channel. However, we also noticed that when the pipette pressure was ~ 300 mBar, the cells were often “blown away” by the pipette even when the pipette tip was somewhat distant from the target cell (e.g., $\sim 10 - 20\ \mu\text{m}$ from the target cell membrane, which corresponded to $\sim 20 - 30\ \mu\text{m}$ distance between the pipette tip and the center of a $20\ \mu\text{m}$ diameter cell). To prevent the pipette blowing away the target cell, we tried a few combinations of distances and pressure values for approaching the target cell. As a result, we found a pressure of ~ 100 mBar to keep the cell in place right until the pipette tip made contact with the cell membrane (contact between the pipette tip and the cell membrane was visually assessed by observing the presence of heartbeat modulation as in Komai et al., 2006; $n = 17$ tdTomato-expressing PV-positive cells from 3 PV-Cre x Ai14 mice). We therefore decided to implement three different pressure values in the brain penetration (Figure 1Biii) and closed-loop real-time image-guided pipette positioning (Figure 1Biv) stages of the imagepatching algorithm while approaching the target cell: (i) 600 mBar for moving the pipette into the brain through upper cortical layers to $75\ \mu\text{m}$ away from the center of the target cell; (ii) 300 mBar for moving the pipette to $25\ \mu\text{m}$ away from the center of the target cell; (iii) 100 mBar for making the final approach to the cell.

Optimization of cell-pipette contact detection, gigaseal formation, and break-in

Akin to manual two-photon image-guided patching (Häusser and Margrie, 2014; Komai et al., 2006; Margrie et al., 2003) and our previously developed blind autopatching method (Kodandaramaiah et al., 2012, 2016), imagepatching uses an increase in pipette resistance as a signal for when the pipette tip contacts the cell membrane. To determine the amount of resistance increase corresponding to a cell membrane-pipette tip contact amenable to a gigaohm seal, we tried forming a gigaseal (by applying slight suction to the pipette and hyperpolarizing the pipette) after observing resistance increases over consecutive z steps (3 μm step size). After a few trials on tdTomato-expressing PV-positive neurons in somatosensory and motor cortices of anesthetized PV-Cre x Ai14 mice, we found that a 20 – 50% increase in pipette resistance, which is the amount visually assessed during manual patching when the pipette tip-cell membrane contact is amenable to gigaseal formation (Häusser and Margrie, 2014; Margrie et al., 2002, 2003), was hard to observe when the increase in resistance was calculated over a single z step (i.e., over 3 μm ; step size of 3 μm was used for single z steps throughout cell-pipette contact detection optimization described below) of a pipette at 100 mBar. This characteristic resistance increase was observable by taking one or more additional steps toward the target cell after seeing some resistance increase over 3 μm , but these extra steps sometimes damaged the cell membrane, resulting in cell lysis. Even when the cell seemed intact, releasing the positive pressure and applying light suction following the 20 – 50% resistance increase over 2 or more consecutive z steps (i.e., over 6 μm or more) did not improve the rate of forming a gigaseal compared to the same pressure modulation following a single z step with less resistance increase, maybe because the pipette tip was pushed too much into the target cell, damaging the cell membrane. As expected, there were instances in which analyzing the pipette resistance over a single z step seemed “noisy,” showing some resistance increase even when the pipette tip was far away from the target cell membrane. However, we could minimize the number of such false positives by analyzing the resistance increase only when the distance between the pipette tip and the cell centroid was small enough that a contact was likely (e.g., the pipette tip-cell centroid distance was less than the radius of the target cell). As a result, we decided to closely examine the resistance increase over a single z step of a patch pipette as the tip of the pipette at 100 mBar was brought in contact with the cell membrane, aiming to determine the amount of resistance increase that subsequently maximized the rate of forming a gigaseal. Since most of the single z steps led to a pipette resistance increase of less than 1% when the pipette tip was far away from the cell membrane, we studied the relationship between the amount of resistance increase of at least 1% over a single z step and the likelihood of successful gigaseal formation. By analyzing 46 gigaseal formation attempts (in 14 mice), in which we released positive pressure and applied suction using the autopatcher control box immediately after observing a resistance increase by 1% or more over a single z step, we found that resistance increases by 4% or more over a single z step led to successful gigaseal formation 22.2% of the time ($n = 4$ gigaseals out of 18 attempts), while single z steps with a resistance increase between 1% and 4% yielded a higher rate of successful gigaseal formation of 32.1% ($n = 9$ gigaseals out of 28 attempts). Out of the 28 attempts with a resistance increase between 1% and 4% over a single z step, we also found that single z steps with a resistance increase between 1 and 2% were more likely to result in successful gigaseal formation (50%; $n = 4$ gigaseals out of 8 attempts) compared to those with higher amounts of resistance increase (e.g., 27.3%, or $n = 3$ gigaseals out of 11 attempts, for single z steps with a 2 – 3% resistance increase; 22.2%, or $n = 2$ gigaseals out of 7 attempts, for single z steps with a 3 – 4% resistance increase). As a result, we decided to use a resistance increase by 1% over a single z step (i.e., an increase by ~ 60 – 70 $\text{k}\Omega$ over 3 μm for 6 – 7 $\text{M}\Omega$ pipettes) as the threshold in the imagepatching algorithm for the detection of contact between the pipette tip and the cell membrane.

Once the pipette tip made contact with the cell membrane, the micromanipulator was halted to keep the pipette stationary, and the pipette pressure was lowered from 100 mBar to 30 mBar to prepare the target cell for gigaseal formation. From a few manual patching experiments, we found that this reduction in pipette pressure led to an increase in pipette resistance by $\sim 1.5\%$ or more when the pipette tip was in close contact with the cell membrane, perhaps because the lower positive pressure allowed the cell membrane, which had been displaced away from the pipette tip due to the higher positive pressure, to spring back toward the pipette tip. In addition to the resistance increase, we could also observe heartbeat modulation of the pipette current pulses as described before (Häusser and Margrie, 2014; Komai et al., 2006; Margrie et al., 2002). The metric used to quantify heartbeat modulation was derived based on our finding during manual patching that, when the pipette tip was in close contact with the cell membrane, current pulses resulting from 50 Hz square waves of injected voltage had a characteristic variation in their resistance values when obtained over 1 s. Specifically, we observed that when the pipette tip at ~ 30 mBar was in tight contact with the cell membrane, the resistance values of 50 current pulses (corresponding to a 1 s long measurement; resistance was calculated by dividing the amplitude of the injected voltage by the amplitude of an observed current pulse) showed a standard deviation of at least 0.1 $\text{M}\Omega$, and a subsequent suction led to a gigaseal ($n = 6$ neurons, 6 mice). We therefore used the standard deviation of the current pulse resistances calculated over 1 s at 30 mBar pipette pressure as a second criterion for detecting contact between the pipette tip and the cell membrane. Even when the resistance increase was less than 1.5% or the amount of heartbeat modulation was less than 0.1 $\text{M}\Omega$, a tight contact amenable to gigaseal formation could be achieved by first increasing the pipette pressure back to 100 mBar (to clear the pipette tip in case it became partially occluded while at 30 mBar) and then advancing the pipette tip by one or more additional z steps until a resistance increase by 1.5% or more was observed. We mimicked this resistance-based check for the pipette tip-cell membrane contact at 30 mBar in the imagepatching algorithm by first performing two consecutive resistance measurements in response to 50 Hz square waves, each for 1 s, then comparing each of the average resistance values (each taken over 1 s) to the pipette resistance observed

before reducing the pipette pressure to 30 mBar, and finally resuming the pipette z steps if the resistance increase was less than 1.5% or if the standard deviation of current pulse resistances was less than 0.1 M Ω (see [Figure S2](#), “closed-loop real-time image-guided pipette positioning,” for details).

After checking the pipette tip-cell membrane contact at 30 mBar, a ramp of suction (–20 mBar/s) was applied to reach a final suction value of –20 mBar, to achieve a gigaohm seal. If the rate of resistance increase was slow (i.e., the pipette resistance measured 10 s after the suction reached the final value of –20 mBar was less than 8 times the resistance measured right before applying the ramp of suction), stronger suction up to –100 mBar was applied in a ramp at –20 mBar/s; negative pressure stronger than –100 mBar was not implemented based on our observation during manual trials that suction levels stronger than –100 mBar did not help to form a gigaseal, but instead led to premature and leaky break-ins. The holding voltage was also set to –65 mV as the seal was being formed. If the pipette resistance did not reach 300 M Ω within 5 s after applying the hyperpolarizing voltage, the pressure level was modulated among 0, 25, and –20 mBar to “coax” the cell membrane into forming a gigaseal. This coaxing process was developed from our manual patching experiments in which alternating the pipette pressure among 0, 25, and –20 mBar led to a gigaseal formation for some of the trials that seemed to be failing (with the pipette resistance increasing very slowly or becoming stagnant following the suction and hyperpolarization), and it was required for 8 out of 42 gigaseals when targeting PV-positive neurons (in 16 PV-Cre x Ai14 mice) and for 4 out of 19 gigaseals when targeting CaMKII α -positive neurons (in 10 CaMKII α -Cre x Ai14 mice) during the imagepatching algorithm validation. If more than 5 min were needed for the pipette resistance to exceed a gigaohm, the pipette was retracted from the brain to start a new trial. Otherwise, the pipette resistance was continuously recorded until it reached a stable value, not increasing by more than 15% over 15 s (see [Figure S2](#), “gigaseal formation,” for details).

The break-in process was developed based on a combination of previously developed protocols ([Häusser and Margrie, 2014](#); [Komai et al., 2006](#); [Margrie et al., 2003](#)) and our experience with manual patching. Three consecutive pulses of suction were applied, with each pulse increasing in suction from 0 mBar to –25 mBar at –20 mBar/s and then returning to 0 mBar. These suction pulses were repeatedly applied every 5 s until the whole-cell configuration was verified with both visual (i.e., the target cell being filled with the pipette dye, indicated by an increase by at least 15% in the mean pixel intensity inside the patched cell boundary in the pipette dye channel) and electrical (i.e., resistance recorded < 250 M Ω) indications. If the whole-cell state could not be achieved after three consecutive pulses, the suction endpoint was lowered by 25 mBar, and suction pulses were again applied to the cell. If a suction endpoint lower than –350 mBar had to be applied, the pipette was retracted to start a new trial. With this algorithm, we were able to achieve the whole-cell configuration successfully from a gigaseal ~57% of the time when targeting PV-positive neurons (n = 24 out of 42 gigaseals in 16 PV-Cre x Ai14 mice) and ~68% of the time when targeting CaMKII α -positive neurons (n = 13 out of 19 gigaseals in 10 CaMKII α -Cre x Ai14 mice) during the imagepatching algorithm validation, where a successful whole-cell state is defined as that with less than 500 pA of leakage current when held at –65 mV in voltage-clamp mode.

Derivation of dye-ejection based pipette blockage test

We derived an algorithm for determining the amount of dye being ejected at the pipette tip, which indicates the pipette tip quality ([Komai et al., 2006](#)), from test images of clean and contaminated pipettes inside the somatosensory and motor cortices of anesthetized PV-Cre x Ai14 mice (3 mice). We used 12 pipettes, angled at 30° below the horizontal, positioned ~150 – 200 μ m deep inside the brain, applying ~300 mBar at the tip, to obtain test images (17x zoom), from which characteristic features were analyzed. We captured images of these pipettes both outside the brain (at ~6 – 8 mBar to make the pipette tip visible) and inside the brain (at ~300 mBar, right after entering the brain at ~600 μ m/s). Out of 12 pipettes, 7 were “clean,” clearly showing the dye being ejected at the tip, while the rest were occluded. By comparing these two groups, we found that all of the images capturing a clean pipette possessed either or both of the following characteristics: (i) the maximum pixel intensity of the image captured inside the brain was at least 2 times higher than the maximum pixel intensity of the image captured outside the brain; (ii) the maximum pixel intensity of the image captured inside the brain was at least as high as the maximum pixel intensity of the image captured outside the brain, and the median of the pixel intensities of the image captured inside the brain was at least 40% of the maximum pixel intensity of the image captured inside the brain. In contrast, none of the blocked pipette images showed the above characteristics. We thus decided to use conditions (i) and (ii) for the pipette tip quality check during the imagepatching operation.

Quantification of PV-positive and CaMKII α -positive cell densities

Z stacks of two-photon images (each z stack with five 223.5 \times 223.5 μ m² images and 10 μ m step between consecutive images) were acquired at a depth of ~100 – 250 μ m in somatosensory or motor cortex of anesthetized PV-Cre x Ai14 mice or CaMKII α -Cre x Ai14 mice. One or more z stacks were acquired per mouse, with each stack at different depth and lateral location within the craniotomy. Cells expressing tdTomato were counted manually from each of the z stacks and then scaled to give the number of cells in a volume of 200 \times 200 \times 100 μ m³.

Input resistance and spontaneous firing rates of imagepatched cells

Input resistance ([Figure S4D](#)) of an imagepatched cell was determined by repeatedly injecting a hyperpolarizing current pulse (–100 pA, 1 s long) to the cell right after achieving the whole-cell configuration, then calculating the average of membrane voltage

over two 100 ms periods (one right before current injection and another at the end of current injection), and finally dividing the absolute value of the difference between the average values of two 100 ms periods by 100 pA. Spontaneous firing rate (Figure S4E) of an imagepatched cell was determined by calculating the frequency of action potentials about 4 to 5 min after break-in over a period of one minute.

QUANTIFICATION AND STATISTICAL ANALYSIS

The statistical details for comparing the recording quality metrics between the imagepatched and fully manually patched PV-positive neurons (Figures S4A–S4C) are provided in the Results section. The p values associated with the Student's t-Test were calculated using *ttest()* function in Excel 2013, with *Tails* parameter = 2 for two-tailed distribution and *Type* parameter = 3 for two-samples with unequal variance.

DATA AND SOFTWARE AVAILABILITY

The Imagepatcher software and the user guide are included as Methods S1.

Neuron, Volume 95

Supplemental Information

Closed-Loop Real-Time Imaging

Enables Fully Automated Cell-Targeted

Patch-Clamp Neural Recording *In Vivo*

Ho-Jun Suk, Ingrid van Welie, Suhasa B. Kodandaramaiah, Brian Allen, Craig R. Forest, and Edward S. Boyden

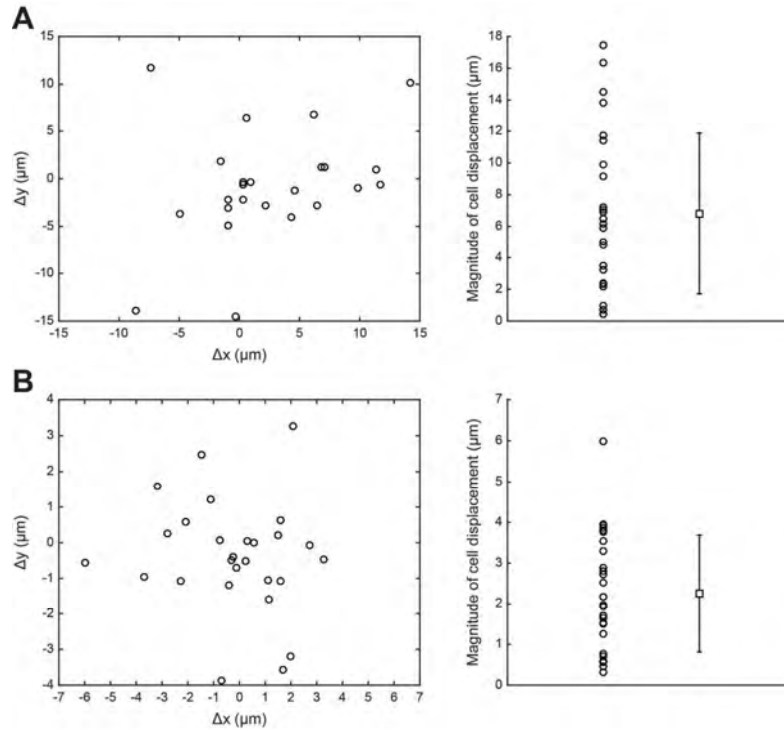
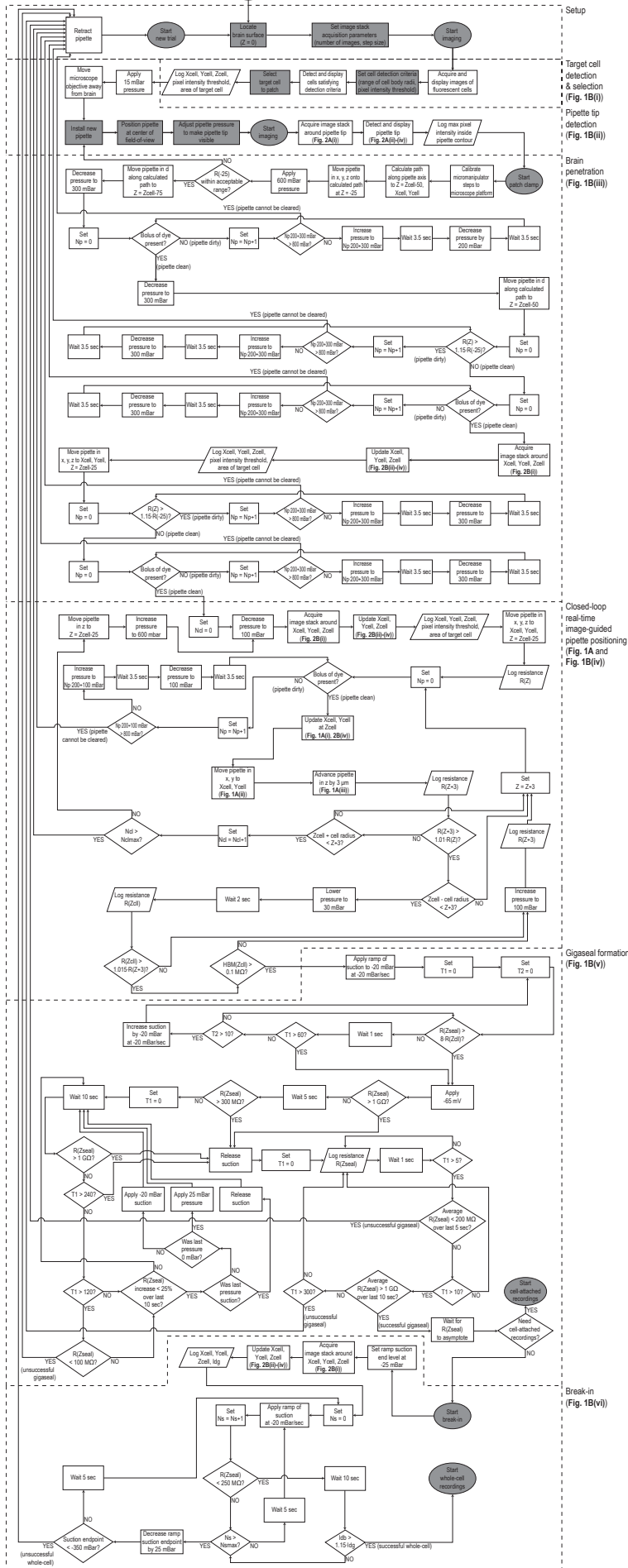
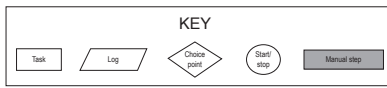


Figure S1, related to Figure 1. Cell movements following pipette navigations into the brain.

(A-B) Target cell displacements in the transverse plane (left) and their magnitude (right), following pipette navigations into the brain. Δx , change in the x coordinate of the target cell centroid, with a positive value corresponding to a cell movement to the right relative to the original location; Δy , change in the y coordinate of the target cell centroid, with a positive value corresponding to a cell movement in the anterior direction relative to the original location. Each circle represents a movement of a single cell, while squares and error bars are mean \pm standard deviation.

(A) Target cell movements following pipette navigation along a linear trajectory parallel to the pipette axis ($n = 25$ cells in 6 anesthetized mice), with the pipette moving from above the brain surface to cortical layer 2/3.

(B) Target cell movements following pipette navigation in the x, y, and z directions ($n = 27$ cells in 17 anesthetized mice), with the pipette moving from a point 20 – 30 μm away from the target cell centroid to a point 10 – 20 μm directly above the target cell centroid.



Setup

Target cell detection & selection (Fig. 1B(i))

Pipette tip detection (Fig. 1B(ii))

Brain penetration (Fig. 1B(iii))

Closed-loop real-time image-guided pipette positioning (Fig. 1A and Fig. 1B(iv))

Gigaseal formation (Fig. 1B(v))

Break-in (Fig. 1B(vi))

Figure S2, related to Figure 1. Step-by-step flowchart, showing the entire imagepatching process.

Dotted lines frame each of the stages of the algorithm; within the dotted line frames, symbols represent task, logging, and choice points, along with text explaining the individual steps and consequences of each decision (see “**KEY**” for definition of symbols). Abbreviations: Z , depth inside the brain, in microns (with more positive Z values indicating deeper positions inside the brain); Z_{cell} , depth of the target cell, X_{cell} , x-coordinate of the target cell centroid at Z_{cell} ; Y_{cell} , y-coordinate of the target cell centroid at Z_{cell} ; x , movement direction along the x-axis of the 4-axis manipulator; y , movement direction along the y-axis of the 4-axis manipulator; z , movement direction along the z-axis of the 4-axis manipulator; d , movement direction along the diagonal axis (i.e., axis parallel to the pipette) of the 4-axis manipulator; $R(Z)$, pipette resistance at depth Z ; N_p , counter for the pipette clearing pressure pulse; N_{cl} , total number of times the closed-loop is run; N_{clmax} , limit on the number of times the closed-loop is run; Z_{cl} , depth at which pipette pressure is lowered to 30 mBar; $R(Z_{cl})$, pipette resistance at Z_{cl} ; $HBM(Z_{cl})$, amount of heartbeat modulation at Z_{cl} ; $R(Z_{seal})$, pipette resistance at the depth at which a gigaseal and the whole-cell state are being achieved, which will vary over time as the algorithm progresses; T_1 , time, in seconds; T_2 , time, in seconds; N_s , total number of times a suction pulse is applied for break-in; N_{smax} , limit on the number of times a suction pulse is applied for break-in; I_d , mean pixel intensity inside the target cell contour, in the microscope channel corresponding to the pipette dye; I_{dg} , I_d when $R(Z_{seal})$ is higher than 1 G Ω ; I_{db} , I_d when $R(Z_{seal})$ is less than 250 M Ω .

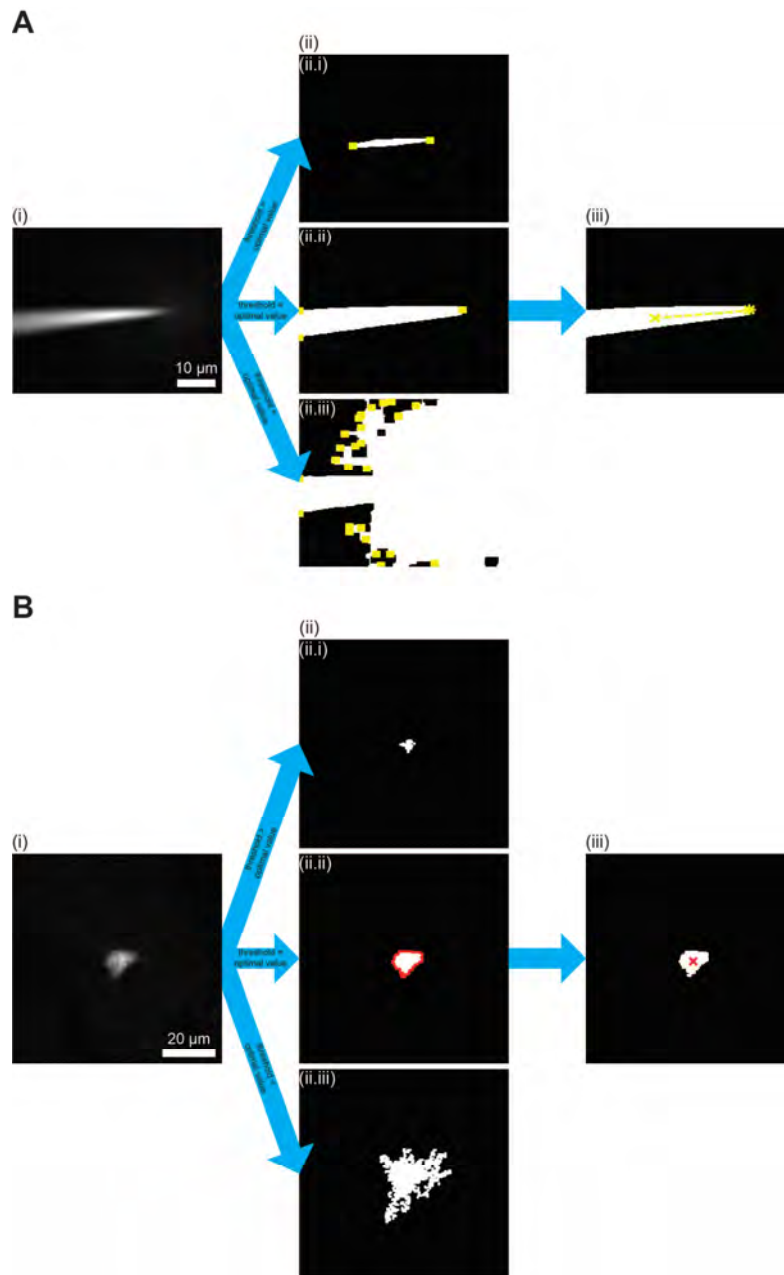


Figure S3, related to Figure 2. 2D image analysis algorithms for detecting pipette tips and cell centroids.

(A) Steps used to detect the tip of a fluorescent dye filled patch pipette from an image focused on the pipette tip. (i) An image of the pipette at the z-coordinate of the pipette tip (i.e., an image focused on the pipette tip) is filtered using a 2D Gaussian filter. (ii) Threshold values corresponding to 5 – 75% of the maximum pixel intensity of the filtered image are applied to the filtered image, and the resulting clusters (white) are subjected to MATLAB’s endpoint detection function (bwmorph function with ‘endpoints’ operation) to identify the endpoints (yellow boxes). Clusters and endpoints resulting from threshold values corresponding to 75% (ii.i), 13% (i.e., optimal threshold value; ii.ii), and 3% (ii.iii) of the filtered image’s maximum pixel intensity are shown as examples. (iii) The cluster resulting from the optimal threshold value is analyzed to locate its

centroid (yellow x) and extrapolate a line from the centroid in the direction of the pipette angle (yellow dotted line). The pixel in the cluster that is closest to the endpoint of the extrapolated line (i.e., endpoint opposite to the centroid) is designated as the pipette tip (yellow star).

(B) Steps used to detect the cell boundary and centroid from each image in a z-stack acquired around a fluorescent cell. (i) An image in a z-stack acquired around a tdTomato-expressing cell is filtered using a 2D Wiener filter. (ii) Threshold values corresponding to 5 – 95% of the maximum pixel intensity of the filtered image are applied to the filtered image, and the resulting clusters (white) are analyzed to determine their areas (i.e., numbers of pixels in the clusters). The cluster whose area is the closest to that of the cell chosen by the user during the target cell detection and selection stage ((ii.i), white) is further processed to determine its boundary ((ii.ii), red outline). Clusters resulting from threshold values corresponding to 50% (ii.i), 20% (i.e., optimal threshold value; ii.ii), and 3.5% (ii.iii) of the filtered image's maximum pixel intensity are shown as examples. (iii) The cluster obtained by applying the optimal threshold value to the filtered image is processed to yield its centroid (red x), designated as the centroid of the cell in the image.

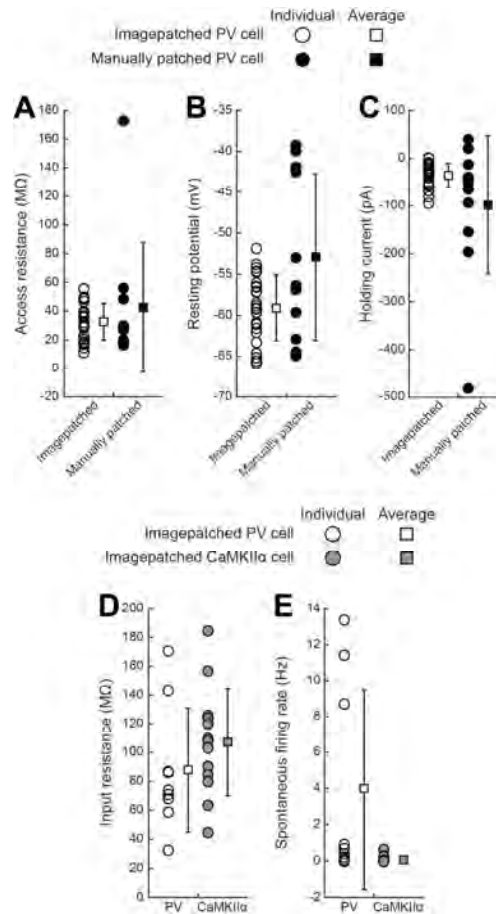


Figure S4, related to Figure 4. Recording quality and electrophysiological properties of imagepatched neurons.

(A-C) Recording quality of imagepatched (white symbols; $n = 24$ cells from 14 mice) vs manually patched (black symbols; $n = 11$ cells from 8 mice) tdTomato-expressing PV-positive interneurons in somatosensory and motor cortices of isoflurane-anesthetized PV-Cre x Ai14 mice. Squares and error bars are mean \pm standard deviation.

(A) Access resistance.

(B) Resting potential.

(C) Holding current.

(D-E) Electrophysiological properties of imagepatched tdTomato-expressing PV-positive neurons (white symbols; 9 cells from 5 PV-Cre x Ai14 mice) and imagepatched tdTomato-expressing CaMKII α -positive neurons (gray symbols; 13 cells from 7 CaMKII α -Cre x Ai14 mice) in somatosensory and motor cortices of isoflurane-anesthetized mice. Squares and error bars are mean \pm standard deviation.

(D) Input resistance.

(E) Spontaneous firing rate.

Failure Modes	PV	CaMKIIα
Pipette Blockage	20.4% (n = 22)	21.5% (n = 14)
Failed Gigaseal Formation	37.0% (n = 40)	43.1% (n = 28)
Loss of Seal During Break-in	16.7% (n = 18)	9.2% (n = 6)
Untargeted Patch	3.7% (n = 4)	6.2% (n = 4)

Table S1, related to Figure 4. Four failure modes of the imagepatcher.

Imagepatching attempts that did not result in successful whole-cell recordings (84 out of 108 attempts targeting PV-positive neurons, from 17 PV-Cre x Ai14 mice; 52 out of 65 attempts targeting CaMKII α -positive neurons, from 10 CaMKII α -Cre x Ai14 mice) can be grouped into 4 failure modes: (i) ‘pipette blockage’ includes imagepatching attempts in which a pipette failed to eject enough dye at its tip or experienced a significant rise in its resistance value after entering the brain or while approaching the target cell; (ii) ‘failed gigaseal formation’ includes imagepatching attempts in which contact between an uncontaminated pipette tip and the target cell membrane, followed by pipette pressure modulation and hyperpolarization, did not result in a gigaseal; (iii) ‘loss of seal during break-in’ includes imagepatching attempts in which application of suction pulses following successful gigaseal formation led to a loss of gigaseal or cell lysis; and (iv) ‘untargeted patch’ includes imagepatching attempts in which an unlabeled cell (i.e., a cell that was not fluorescently tagged), sitting right on top of a targeted cell, was patched instead of the target cell.

Target Cell Depths Below The Brain Surface	Success Rates			
	PV		CaMKII α	
	Gigaseal	Whole-cell	Gigaseal	Whole-cell
≥ 100 and < 200 μm	50.0% (n = 24 out of 48)	29.2% (n = 14 out of 48)	40.0% (n = 14 out of 35)	25.7% (n = 9 out of 35)
≥ 200 and < 300 μm	48.6% (n = 18 out of 37)	27.0% (n = 10 out of 37)	31.3% (n = 5 out of 16)	25.0% (n = 4 out of 16)

Table S2, related to Figure 4. Success rates at different target cell depths, for trials that entered the closed-loop stage of imagepatching.

One unsuccessful attempt targeted a PV-positive cell at a depth below 300 μm and is not included in the table.

PV			CaMKII α		
Number of Labeled Cells in 200 x 200 x 100 μm^3 Volume	Success Rates		Number of Labeled Cells in 200 x 200 x 100 μm^3 Volume	Success Rates	
	Gigaseal	Whole-cell		Gigaseal	Whole-cell
<6	42.1% (n = 8 out of 19)	31.6% (n = 6 out of 19)	<20	40.0% (n = 4 out of 10)	30.0% (n = 3 out of 10)
≥ 6 and <10	57.1% (n = 16 out of 28)	32.1% (n = 9 out of 28)	≥ 20 and <35	30.8% (n = 4 out of 13)	15.4% (n = 2 out of 13)
≥ 10 and <14	33.3% (n = 8 out of 24)	20.8% (n = 5 out of 24)	≥ 35 and <65	47.1% (n = 8 out of 17)	35.3% (n = 6 out of 17)
≥ 14	66.7% (n = 10 out of 15)	26.7% (n = 4 out of 15)	≥ 65	27.3% (n = 3 out of 11)	18.2% (n = 2 out of 11)

Table S3, related to Figure 4. Success rates for different labeling densities of cells around a target cell, for trials that entered the closed-loop stage of imagepatching.

The number of labeled cells around a target cell in a 200 x 200 x 100 μm^3 volume was determined by scaling the number of tdTomato-expressing cells in a z-stack (5 images, 10 μm step size, field of view of 223.5 x 223.5 μm^2) that captured the target cell near the center of its field of view.